NON-DESTRUCTIVE BIOMECHANICAL TESTING OF TISSUES USING A VIBRATIONAL OPTICAL COHERENCE TOMOGRAPHY SETUP

By

RUCHIT GIRISHCHANDRA SHAH

A dissertation submitted to the

School of Graduate Studies

Rutgers, The State University of New Jersey

In partial fulfillment of the requirements

For the degree of

Doctor of Philosophy

Graduate Program in Biomedical Engineering

Written under the direction of

Frederick H. Silver

And approved by

_____

_____

_____

_____

New Brunswick, New Jersey

January, 2018

ABSTRACT OF THE DISSERTATION

NON-DESTRUCTIVE BIOMECHANICAL TESTING OF TISSUES USING A VIBRATIONAL OPTICAL COHERENCE TOMOGRAPHY SETUP

By **RUCHIT GIRISHCHANDRA SHAH**

Dissertation Director:

Frederick H. Silver

The mechanical properties of tissues and implants contribute to their physiological functionality, and have been vast areas of research in fields such as Dermatology, Cardiology, Neurology, Ophthalmology, Orthopedics and Urology. Several tests and modalities have been used to measure the mechanical properties of tissues and implants including tensile, compressive, shear, and bending in one or more axial directions. However, majority of these tests are destructive, rendering the material unusable post-testing; whereas most of the non-destructive imaging modalities such as magnetic resonance imaging (MRI), nuclear magnetic resonance (NMR) and ultrasound are costly and have lower spatial resolution. Optical coherence tomography (OCT) is an optical imaging modality that provides high-resolution images and has been extended to optical coherence elastography (OCE) in various embodiments to compute the mechanical properties of biological tissues. The application of elastography in computing biomechanical properties of tissues such as elastic moduli generally excludes the viscosity component of the tissues. The computation of viscoelastic properties using OCE is still in a nascent stage but has a promising future.

The primary goal of this dissertation was to develop and engineer a vibrational OCT system that performs nondestructive computation of viscoelastic properties of monophasic and composite biological tissues and implants. The underlying hypotheses of this dissertation are: i) the modulus of a tissue computed by using its resonant frequency will be comparable to its elastic modulus obtained from the uniaxial tensile testing method; ii) the resonant frequency and thereby the computed modulus will vary with strain; iii) tissues will demonstrate elastic and viscoelastic properties when pulse-vibrated at resonant and non-resonant frequencies, respectively; and iv) the moduli obtained from the vibrational OCT setup will differ between healthy and diseased tissues.

To validate the efficacy of vibrational OCT system to measure elastic modulus of mono- and multi-phasic biological tissues, a benchtop OCT system with an external speaker was set up to vibrate clamped samples with a continuous sinusoidal force at different strains. The resonant frequency of the samples was identified by observing the speaker-induced tissue displacements over a frequency range of 50 to 1000Hz, and their physical dimensions were used to determine their elastic moduli using the vibrational setup. These moduli were almost identical to those obtained using the gold standard method of uniaxial tensile testing. Multiphasic samples (bovine cartilage and pigskin) exhibited multiple resonant peaks.

In order to compute viscoelastic properties of tissues, the calibrated vibrational OCT setup was modified to generate a burst of 3 cycles of sinusoidal input waves. The samples demonstrated response similar to that of an underdamped system. The half-power bandwidth method was utilized to determine the loss modulus percent of the samples at different strains. The results showed that the viscous component of the dermis is strongest under 100Hz and that the materials exhibit almost purely elastic response at resonant frequencies.

The vibrational OCT setup was also used to characterize/ differentiate chorionic plate tissues from human placentas belonging to early term, normal and abnormal pregnancies. Each group showed distinct biomechanical properties reflecting altered tissue compositions across time and disease state.

ACKNOWLEDGEMENTS

The journey to this dissertation has been an overwhelming one, and has definitely had its share of ups and downs. I would not have been able to make it without the support of a lot of special people in my life. I would like to start by thanking my research advisor, Prof. Frederick Silver, for providing me the opportunity to work on this project and complete my Ph.D. after an untimely break. His vast knowledge and expertise have helped me grow as a researcher over the years. I am also grateful to Prof. Mark Pierce for his invaluable guidance and inputs on this project, for letting me use his lab for my dissertation work, and for being on my committee. I would also like to thank Prof. Nada Boustany for agreeing to be on my committee, and for her deep insights on this project. I extend my sincere thanks to Dr. David Shreiber and Mr. Lawrence Stromberg from the Biomedical Engineering department at Rutgers for all their help in reinstating me as a part-time Ph.D. student and allowing me to complete my Ph.D. I would also like to thank Dr. Dale DeVore for providing the dermis samples used in this study.

I would like to give special thanks to Dr. Carolyn Salafia, my employer at Placental Analytics, LLC, who supported me when the chips were down. I will be forever grateful for your belief and confidence in me to work with you, for not giving up on me and bringing me back to the USA, and motivating me to complete my Ph.D. This certainly would not have been possible without your support and understanding. I have learned so much from you, not only as a researcher but also as a person. Your endless dedication continues to inspire me to keep pushing forward. You have been a great role model and a mentor, and I hope to never let you down. Also, thank you for the placental samples used in this project. I would also like to thank all my friends and colleagues at Placental Analytics and Institute for Basic Research for their help and support.

Last, but definitely not the least, I dedicate this dissertation to my family, especially my loving wife, Shruti, and my parents, Smita and Girish Shah. My family members have been the pillars of my strength and this degree would not have been possible without their trust, support, prayers, sacrifices and blessings. I will be indebted to them for my life. And above all, I am thankful to God for giving me the ability, inspiration and endurance to pursue my dreams.

TABLE OF CONTENTS

LIST OF ABBREVIATIONS

MRI – Magnetic Resonance Imaging

NMR – Nuclear Magnetic Resonance

OCT – Optical Cohesion Tomography

OCE – Optical Coherence Elastography

ECM – Extracellular matrix

UE – Ultrasound Elastography

MRE – Magnetic Resonance Elastography

NIR – Near-infrared

SD-OCT – spectral-domain optical coherence tomography

AFM – Atomic force microscopy

ARFI – Acoustic Radiation Force Impulse

SWI – Shear Wave Imaging

1D-TE – 1-dimensional transient elastography

pSWE – point shear wave elastography

2D-SWE – 2-dimensional shear wave elastography

PDMS – Polydimethylsiloxane

SDOF – single degree of freedom

PBS – phosphate buffered saline

LIST OF TABLES

LIST OF ILLUSTRATIONS

CHAPTER 1: INTRODUCTION

The overarching aim of this dissertation was to develop and validate a nondestructive technique to measure viscoelastic properties of biological tissues based on their resonant frequencies using a vibrational OCT setup. This chapter provides the background and motivation behind this dissertation. It begins with an overview of the molecular and fibrillar basis of the mechanics of collagen and skin, followed by the importance of biomechanical testing of tissues and the shortcomings of the most commonly used methods of performance of biomechanical testing. This is followed by a discussion of the basic principles of OCT and some of its current biomedical applications. The basics of the human placenta are then introduced along with the importance of studying its biomechanical properties.

Structure and function of skin

Skin, the largest organ of the human body, is a complex multilayer tissue that mainly consists of two layers: epidermis and dermis (**Figure 1**) [1]. The epidermis that serves as the main protectant from environmental influences is a 75-150μm thick layer that mainly comprises outward migrating cells known as keratinocytes. The other cells found in the epidermis are melanocytes, Langerhans cells and Merkel cells [2]. The dermis is an extremely soft and viscous fibroelastic connective tissue layer that spans 1-4mm in depth and performs the primary physical, physiological, neurological and metabolic functions [1]. It constitutes the bulk of the human skin and contributes to 15-20% of the total body weight and consists of collagen, elastin, reticulin and a supporting matrix. Collagen comprises about 75% of the fat free dry weight and 18-30% of the volume of dermis [2,3]. A network of elastin is interspersed among the bundles of collagen that restores the normal fibrous array post- deformation caused by external mechanical forces. The undulated collagen fibrils get straightened at higher extension rates. The supporting matrix is composed of

glycosaminoglycans, long chains of polysaccharides that form a gel that retains moisture in the dermis, even under high pressure. The thickness of each skin layer varies with age, anatomical location and/or hydration [4].

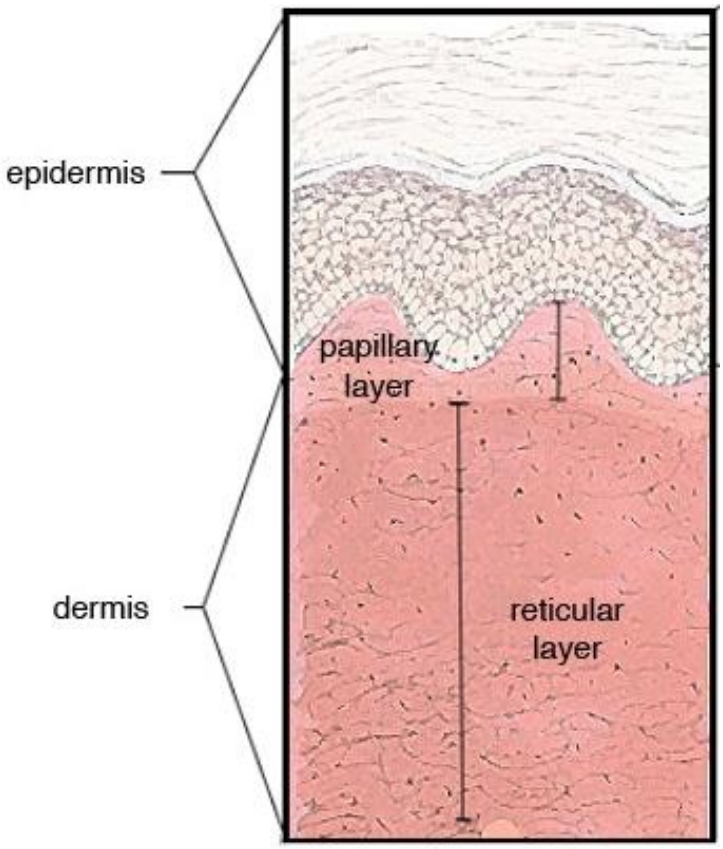

Figure 1. Different layers seen under a cross-section of human skin

The dermis can be further subdivided into two anatomical regions: the papillary dermis and the reticular dermis (**Figure 1**). The papillary dermis is the thin outermost layer of dermis comprising smaller and loosely distributed elastic and collagen fibrils, and constitutes ~10% of its thickness. The reticular dermis constitutes the greater bulk of the dermis and contains dense collagenous and elastic connective tissue with a relatively small quantity of cells and veins.

The human skin serves several functions including: a) protection from physical, biological and chemical external influences; b) maintenance of homeostasis and water balance through thermoregulatory secretory activity; c) transmission of information about external influences obtained through sensory reception; d) biochemical synthesis of essential vitamins and hormones. Furthermore, the skin also plays a minor role in the respiration through the exchange of gases with the environment [5]. The interwoven network of collagen and elastic fibers, along with fibroblasts, hair follicles, sweat glands, and neural circuitry, provide skin the structural and mechanical support, and subsequently allow it to perform its crucial functions [1]. The shape-defining characteristic of the skin is largely a result of its macromolecules including elastin and collagen [1,6]; whereas the collagen fibrils in the upper and lower layers of dermis are responsible for the storage of mechanical energy associated with gravity or impact loads and transmission and dissipation of this energy [6–9].

Almost 70-80% of skin's dry weight constitutes of collagen, and ~80% of that total collagen content is type I collagen; type III collagen accounts for 15%, and the remaining 5% are of other collagen types, including IV, V, VI, VII XII, and XIV [6,10]. Collagen types I and III form the base of the fibril network and are responsible for most of the skin's mechanical properties. The other collagen components provide stability to the skin and are affected by mechanical loading. Prevention of tissue failure by withstanding deformation and energy dissipation is the major function of the collagen fibers and the structures formed by them [1,11–15].

Human skin is viscoelastic as evident from the biphasic response of typical stress–strain curves comprising linear low- and high-strain regions [10,14,15]. Skin primarily behaves as an elastic material in the low-strain or toe region. This behavior is attributed to the elastic fibers that recover small strains in the collagen network [9,11,14]. Straining the

tissue beyond the toe region, aligns the collagen fibrils and employs them to absorb and store the strain energy [14–17]. At higher strains, a viscous component is implicated in the energy dissipation of an applied load through molecular sliding of collagen fibrils in the extracellular matrix (ECM) [12,14,15]; whereas, the elastic component is responsible for shape recovery after deformation by axial stretching of the triple helix and energy storage through the changes in the pitch of the triple helix caused by the stretching of flexible regions in the collagen triple helix [12,14,15]. Electrostatic interactions among the charged residues of the flexible regions of the collagen triple helix have also been associated with other significant functions of skin such as mineralization and signal transduction [18].

This viscoelastic nature of the skin presents a considerable challenge in testing its biomechanical properties. Various techniques have been developed for *in vivo* and *in vitro* biomechanical testing of skin; however, different experimental conditions alter the natural state of the skin differently and thereby report elasticity values with vast discrepancies [19–21]. This calls for a need of a testing method that can measure the biomechanical properties of the skin whose results correlate with those of standard tensile testing methods.

Collagen

Collagen is a major protein found in all connective tissues including bone, skin, tendon and cartilage. They are a large family of structural proteins found in the ECM of all vertebrates and invertebrates and account for one-third of ECM's total protein mass [22]. They not only provide the structural support but also impact cellular behavior and gene expression via interactions with other matrix proteins and receptors.

Each of the collagen types plays a unique structural role in the ECM. However, all of them have the characteristic triple helical component as a part of their structure. Type I, II and III form fibrils are the most abundant collagens and have continuous gly-X-Y amino acid

repeats of ~1000 amino acid residues. Other collagen types contain smaller continuous regions of gly-X-Y in their triple helices and are collectively termed as non-fibrillar collagens that play a role either in association with the fibers (fibril associated collagens with interrupted triple helices), in networks (e.g.: types IV and VIII) or in linking structures (e.g. type VII). In mammals, individual collagen triple helices, known as tropocollagen, assemble in an intricate, hierarchical manner and eventually lead to macroscopic fibers and networks found in tissue, bone, and basement membranes (**Figure 2**) [23]. The structural hierarchy and mechanical properties of type I collagen vary for different tissues; however, the ultimate tensile strength of tissues containing type I collagen has been shown to correlate with fibril and fiber diameters [24].

Mechanochemical transduction is the process that influences the biochemical and genetic responses of cells and tissues through external forces such as gravity. Specifically, these responses include stimulation of cell proliferation or apoptosis, and synthesis or catabolism of the ECM components [25]. These processes lead to either an increase the in chemical energy (conversion of amino acids or other small molecules into macromolecules) or a decrease in chemical energy (depolymerization of macromolecules).

Collagen fibers are essential for vertebrates to achieve effective locomotion, and for tissue regeneration and repair through mechanochemical transduction [12,14–16,25–28]. For effective locomotion, vertebrates should be able to develop muscular forces, store elastic energy, and transfer this energy to the attached joints. Furthermore, they should be capable of transferring the post-movement residual energy from the joints back to the muscles where it can be dissipated as heat [25,29]. During the normal gait cycle in vertebrates, the tendons that are stretched post-impact with the ground store potential energy as strain energy. Additionally, elastic recoil by these tendons converts most of the

stored energy into kinetic energy [30,31]. Normal aging, and wear and tear from diseases involving ECM collagens are commonly associated with a decreased energy storage and dissipation [28,32]. Energy storage, transmission and dissipation in ECMs are closely related to molecular changes to collagen molecules, fibrils, and fibers [25].

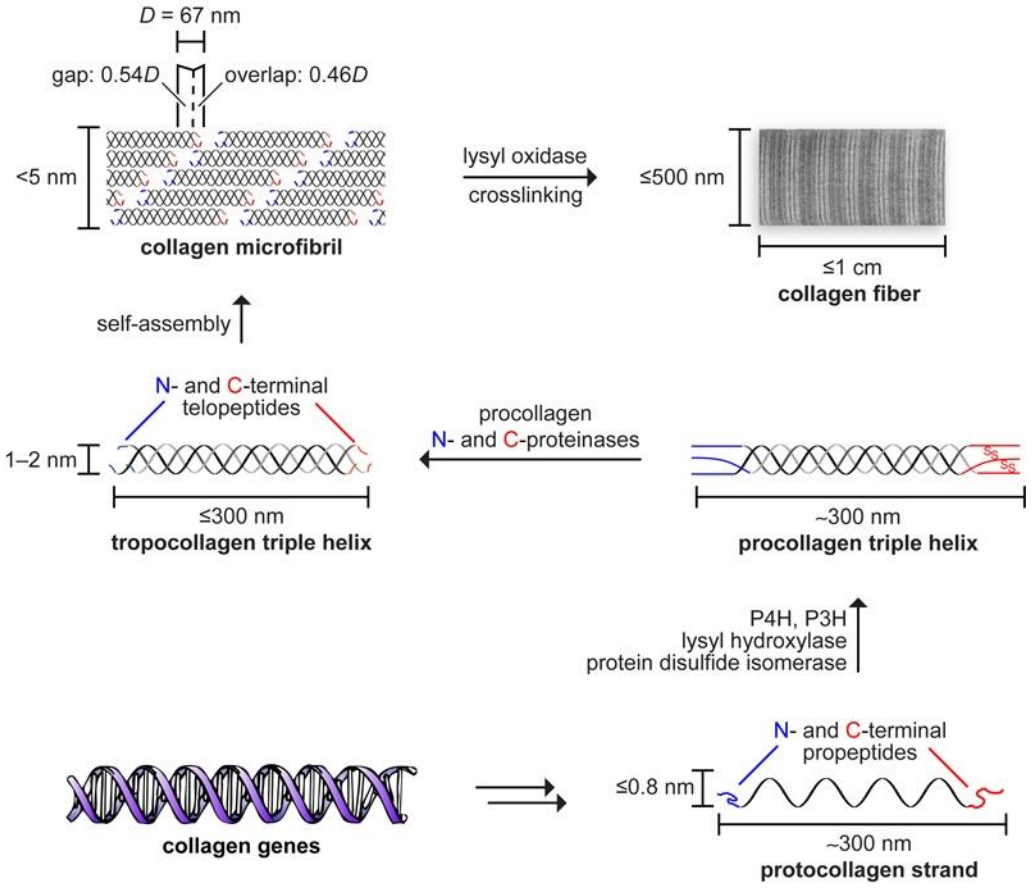

Figure 2. Biosynthetic route to collagen fibers *[33]*, which are the major component of skin. Size and complexity are increased by posttranslational modifications and self-assembly. For fibrillar collagens, the ~ 300nm long triple helical molecules are staggered by ~ 67nm, a length known as D period, to form a quarter-staggered structure known as a collagen microfibril. The distance D, a characteristic fingerprint of a fibrous collagen, is made up of a hole region of about 0.6D and an overlap region of about 0.4D [Adapted from Shoulders and Raines, 2009]

Collagen fibers are viscoelastic and portray time-dependent mechanical behavior. Viscoelasticity may play in important role in helping collagen in musculoskeleton to prevent impact loads; however, it complicates studying the ECM behavior as most real-time tests on these tissues contain both elastic and viscous contributions [14]. The elastic behavior of collagen fibers depends on their orientation, rate of loading and quantity of other constituents in the tissue and can range from as high as about 90% of the total stress for tendon to as low as about 50% for skin [14].

Collagen properties including non-toxicity, quick resorption into the body, promotion of cell attachment and interaction within cells, providing direction of cell orientation and minimal immune response even when transplanted into hosts from different species, make it an ideal biomaterial. Moreover, it can be fabricated in various forms such as sheets, gels etc., and can be chemically crosslinked or combined with other biological or synthetic materials to alter its mechanical properties or cell behavior to specific applications of interest [34,35].

Collagen is a commercial medical product that can be a part of a medical device or reconstituted from different sources and be used for various biomedical applications like tissue engineering and cosmetic surgery. Collagen has found applications in various medical fields like wound dressings, tissue augmentation in dermal applications, bioprosthetic heart valves in cardiology, collagen based sutures in surgery and even in treatment of urinary incontinence [36]. Collagen is typically extracted from human cadavers or animal sources especially bovine for most of these applications. However, there is a need for reliable biomechanical testing methods for assessing the properties of these allografts and xenografts post-treatments that alter their biological properties and/or sterilize them.

Biomechanical Testing

ECMs are multicomponent tissues that transduce internal and external mechanical signals into changes in tissue structure and function through a process termed mechanochemical transduction [25,26,37]. Mechanical loading plays a vital role in vertebrate development, evolution, tissue maturation and development of tissue fibrosis during wound healing [26,27,38–42]. Abnormal mechanochemical transduction processes may also lead to tissue fibrosis in diseases such as osteoarthritis [27] and cancer [43]. Since the fibril-forming collagens are the major structural components of ECM, it is important to understand the mechanical properties of fibrous collagen.

Various *in vitro* and *in vivo* techniques have been used to evaluate the mechanical properties of biological tissues over the last four decades [8,14,44–48]. Classical *in vitro* techniques include tensile, compressive, torsional and bending methods, and use various loading and/or unloading settings such as constant rate-of-strain deformation and incremental stress-strain analysis. The results obtained from *in vitro* techniques are most reliable and can provide basic estimates of mechanical properties like strength, elasticity or density inherent to tissue architecture. However, they are destructive to the tissue and also have a limited translation to the *in vivo* state, where the complex interactions of the tissue with its surroundings need to be considered. *In vivo* testing methods can be majorly divided into static (single modulating stimulus) and dynamic (cyclical stimulus or moving test sample) testing methods. The static testing methods employ uniaxial and biaxial tensile, indentation and rotational straining methods. The dynamic testing methods include ballistometric test [49], shear wave propagation [50], mechanical impedance test [51] and dynamic suction tests [52]. The results of some of these techniques are not in the form of modulus, but rather in terms of other physical parameters like velocity [50]. Moreover, most of these techniques make assumptions such as linear elasticity of the test material,

Poisson's ratio being close to 0.5 and that viscoelasticity does not dramatically affect the resulting properties [53–55]. However, most biological tissues (e.g. skin) are non-linear and viscoelastic in nature, resulting in vast discrepancies in the values of moduli reported in the literature [14,15,55–57]. Also, the upward curvature to their stress-strain curve makes a determination of stiffness very difficult since the tangent to the stress-strain curve is constantly changing [14,45,58]. For most of the cases, these assumptions are tolerable and help to get some sort of basic measure of the biomechanical properties of tissue like strain or shear velocity or stiffness relative to the surrounding tissues. However, in some cases like a host tissue-implant interface or a local tumor, it is crucial to be able to differentiate the normal and abnormal mechanical properties with greater precision and better resolution. The measurement of absolute mechanical properties becomes imperative in such cases where e.g. an excision of a tumor is based on the diagnosis of soft and hard tissue parts.

There is a need to be able to characterize the mechanical properties of human tissues such as skin since this would provide clinicians valuable information concerning the mechanical properties of skin with respect to location and the directions of Langer's lines [59]. In addition, changes associated with tumor formation, wound healing, scarring and the efficacy of cosmetic and surgical treatments could be evaluated quantitatively.

Implants

Beyond the need to mechanically characterize human tissues, it is essential to be able to characterize implants that are used as replacements or to augment tissues [45]. Millions of allografts, xenografts and synthetic implants are used each year for applications that include: bladder regeneration [60], burns [61], breast reconstruction [62], facial cosmetic defects [63], hernias [64], ophthalmic defects [65], oral defects [66], cardiovascular tissue replacement [67], tendon/ligament repair [68], and vaginal repair [69]. While many studies

highlight the use of dermal allografts, questions arise about the effects of processing conditions (e.g.: decellularization, decontamination, and viral deactivation) on the structure of these tissues and the surgical outcomes. While the bulk of polymers used in medicine include polyglycolic acid, polylactic acid, polydimethylsiloxane, polytetrafluoroethylene, polyethylene, polyacrylates, polyurethanes and natural polymers such as collagen, hyaluronan, alginates and silk [45], their properties vary extensively depending on how they are compounded and processed. The use of tissue-derived collagen scaffolds for human surgical applications necessitates removal of cellular components of the epidermis and dermis before processing into the required forms (e.g.: sheets) [70,71]. Changes in the physical structure and mechanical properties occur during tissue decellularization process that may affect the resulting strength and healing properties of these materials.

Another consideration is that most allografts do not have the direction of Langer's lines marked, making it difficult for the surgeon to orient the collagen fiber in the allograft with that of the host tissue. The surgical revisions required due to mechanical mismatches at the implant-tissue interface and failures result in additional surgical costs of billions of dollars every year in terms of lost work time and increased health care expenses. The alignment of the host tissue and allograft Langer's lines is necessary to minimize stress concentration at the interface the failure of which can lead to cellular invasion and remodeling of the allograft and may eventually cause premature graft failure due stress concentrations and up-regulation of mechanotransduction [25]. Additionally, the deformability of decellularized dermis in the direction perpendicular to Langer's lines is much lower than normal skin (10-15 % versus in excess of 40% in skin). This can lead to stress concentration and excess host tissue deformation at the implant-tissue interface.

The current state of biomechanical testing of implants and allografts in mostly destructive mechanical testing [72,73]. The availability of a nondestructive biomechanical testing apparatus can help the clinicians and surgeons to test the implants in the same room and get a clear understanding of the strength and stiffness of synthetic sutures, wound dressing materials, bandages, vascular grafts, and artificial valves are essential to prevent premature mechanical failure of medical devices and implants.

OCT

OCT is an imaging modality that provides noninvasive real-time cross-sectional images of complex media with a resolution of <15μm and a depth of 2-3mm [74]. The OCT images are of higher resolution as compared to MRI or ultrasound, making it of particular interest in biomedical applications like histopathological, ophthalmic, cardiologic and cancer diagnoses [53,75–79]. OCT images are generated by computing the differences in backscattered light of the underlying tissue structures in response to a near-infrared (NIR) beam [75,79,80].

The principles of OCT are often compared to those of ultrasound. With ultrasound, a sound wave is transmitted into the tissue, and the echo time delays and amplitudes of the backscattered sound wave that are the characteristics of the sample's internal structures are determined [79]. With OCT, a NIR light is transmitted and the refractive index mismatch between different structural components of the tissue lead to detectable differences in backscattered light intensity [79]. The significantly higher speed of light makes it impossible to directly measure the echo time delay, as is done in ultrasound [79]. Thus, low-coherence interferometry is used to evaluate the echo time delay by comparing the light received from the sample and a reference path of known length and time delay [79]. A single "A-line" of the sample is acquired by modifying the reference path length [81], and an image ("B-scan") is generated by collecting multiple A-lines across the

sample; both of these factors result in a slow acquisition time of a few frames per second [81,82].

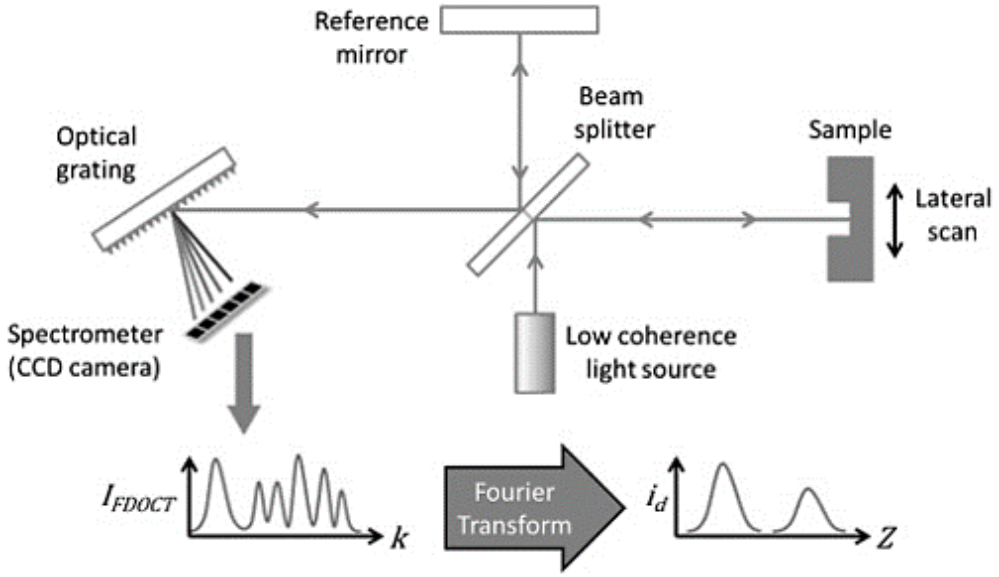

Figure 3. Working of SD-OCT system. The light from a low coherence light source is split and collected back to the beam splitter. The reference arm consists of a stationary mirror. The grating-based spectrometer measures the interference signal as a function of wavelength, λ. The spectral data is rescaled and resampled evenly in k-space, before it is Fourier transformed to get the sample depth profile or A-scan. A lateral scan captures multiple A-scans and creates a cross-sectional image or a B-scan.

Obtaining real-time imaging with reasonable resolution and acquisition rates using this time-domain approach requires mechanically and optically complex reference arm designs [83]. This can be overcome by using the Fourier Domain OCT, where the interferometric signal is acquired as a function of optical wavenumber [81,83,84]. This can be achieved by either using: 1) a broadband light source with a spectrometer for detection ("spectral-domain OCT" or SD-OCT, **Figure 3**), or 2) a single photodiode detector with a wavelength-swept narrowband light source ("swept-source OCT" or SS-OCT) [82]. Both the approaches yield an interferometric signal as a function of optical wavenumber, I(k),

and taking the Fourier transform of I(k) gives backscattered intensity as a function of depth, I(z) [82,84], and consequently generate an A-line. By transverse scanning, multiple A-lines can be acquired to produce a final cross-sectional image.

The use of a broadband light source in SD-OCT makes it possible to obtain the backscattered intensity as a function of depth for the entire length of an A-line all at once, without the need to scan the reference arm as in time-domain OCT (**Figure 3**). As mentioned earlier, many A-lines can be collected by transverse scanning of the source beam and produce a B scan or image, or even a volumetric data by scanning in the third dimension. The simultaneous acquisition of all the intensities of complete A-line significantly speeds up acquisition time, making SD-OCT more sensitive to detection of weak signals, and thereby more suited for clinical applications [84].

Elastography

Elastography utilizes medical imaging to measure the tissue deformation from an applied load and relates the deformation to a mechanical property like stiffness or elasticity, which is then mapped onto an image. Techniques including ultrasound elastography (UE), magnetic resonance elastography (MRE), OCT and OCE have been used to study the dynamic mechanical properties of tissues in health and disease [75,80,85–91]. Initially developed for ultrasound [92] and later on for magnetic resonance [87], elastography is now clinically used for applications such as monitoring of liver disease [93] and diagnosis of breast lesions [94]. The spatial resolution of these techniques ranges from a tens of micrometers [95] to several millimeters [86], allowing visualization of micro- and macro-scale tissue features.

Palpations have been a time-tested diagnostic tool for physicians to feel and differentiate abnormal and normal tissues based on their mechanical properties that widely vary among different physiological and pathological states. For instance, the use of palpation to detect

the relative hardness of malignant breast cancer tumors [96] and the use of a simple touch by the surgeons at laparotomy to detect liver tumors that may have been undetected in preoperative imaging [97]. However, palpation is applicable only to external organs and pathologies, except in case of surgeries, and is qualitative and highly subjective. The inability of the conventional medical imaging techniques, such as computed tomography, MRI and ultrasonography of depicting the properties that are assessed by palpation has motivated the development of special imaging technologies for quantitative assessment of the mechanical properties of tissue.

Magnetic Resonance Elastography

MRE is capable of noninvasive assessment of tissue stiffness and has already been shown to be beneficial as a clinical tool for the diagnosis of hepatic fibrosis [98] along with other potential applications like brain MRE [99] for assessing brain tissue stiffness information that may be related to diseases like Alzheimer's disease, hydrocephalus, brain cancer and multiple sclerosis, skeletal muscle MRE to detect a difference in the stiffness of muscles with and without neuromuscular disease [100], breast MRE (**Figure 4**) for breast cancer diagnosis [101,102].

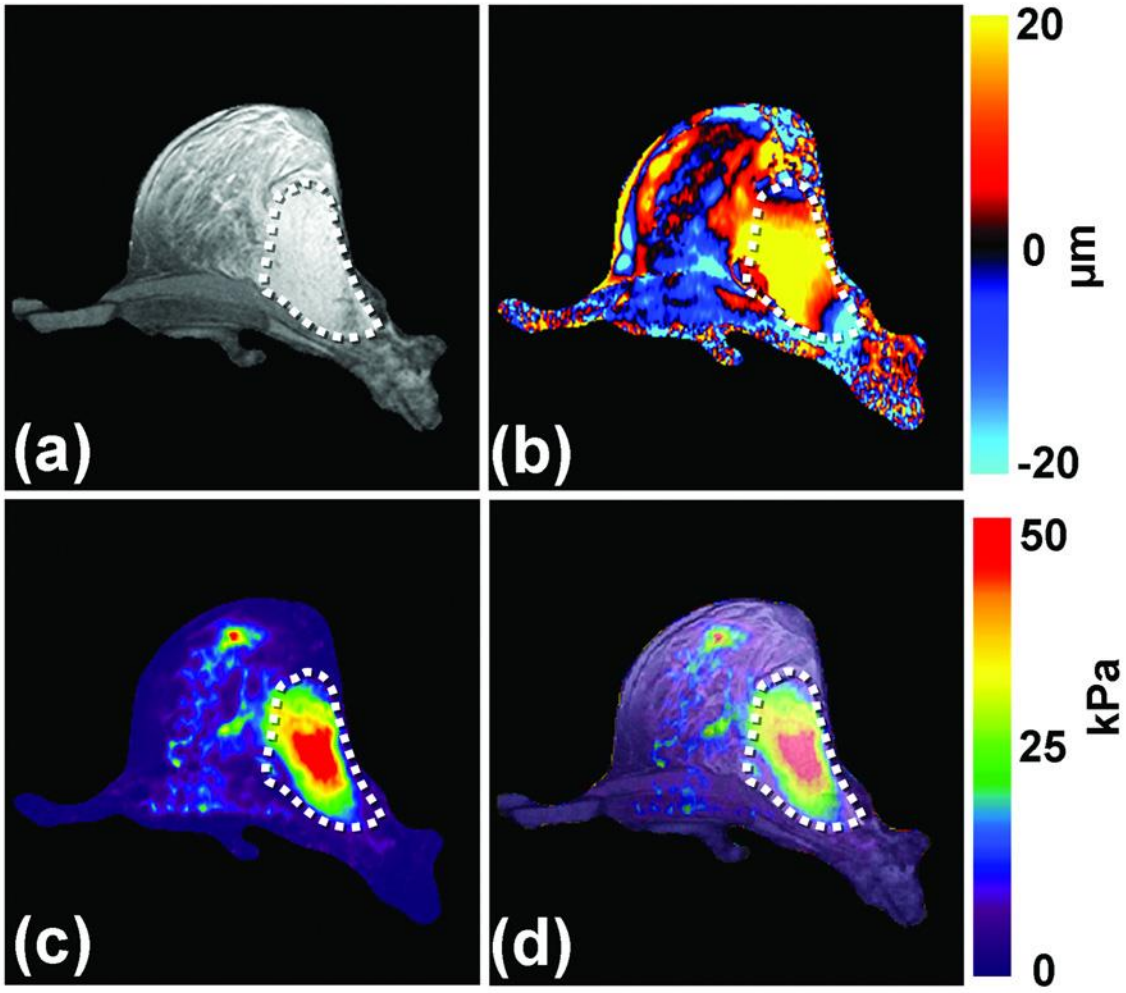

Figure 4. Breast MRE (a) an axial MR magnitude image of the right breast of a patient. A large adenocarcinoma is shown as the outlined, mildly hyperintense region on the lateral side of the breast. (b) A single wave image from MRE performed at 100 Hz is shown along with the corresponding elastogram (c). (d) An overlay image of the elastogram and the magnitude image shows good correlation between the tumor and the stiff region detected by MRE. (Reproduced from Mariappan et al., 2010)

MRE has evolved as a consistent, non-invasive technique that produces high-contrast elastograms with a large field of view that are of great clinical importance (e.g. **Figure 4**). The mechanical parameters computed from MRE are stiffness, shear velocity and

elasticity modulus. New technological advances have made it possible to obtain the elastography measures overlaid on the MRI images in a matter of a few minutes. They have become the state-of-the-art for detecting liver fibrosis [98,103], and have led to a development of commercial MRE instruments like Siemens MAGNETOM™. However, there are some technical challenges that prevent the use of MRE from being used as an assessment tool for other clinical applications. The spatial resolution of MRE is in mm range (**Figure 5**) and it increases further as the frequency of applied shear waves increases. This restricts the use of MRE for smaller tissues where a better spatial resolution is required. Secondly, stiffer tissues like bones and cartilages require a higher vibration frequency that the current MRE systems cannot handle. Additionally, MRE inherits all the other common problems associated with MRI like high-cost and potential claustrophobia for obese patients.

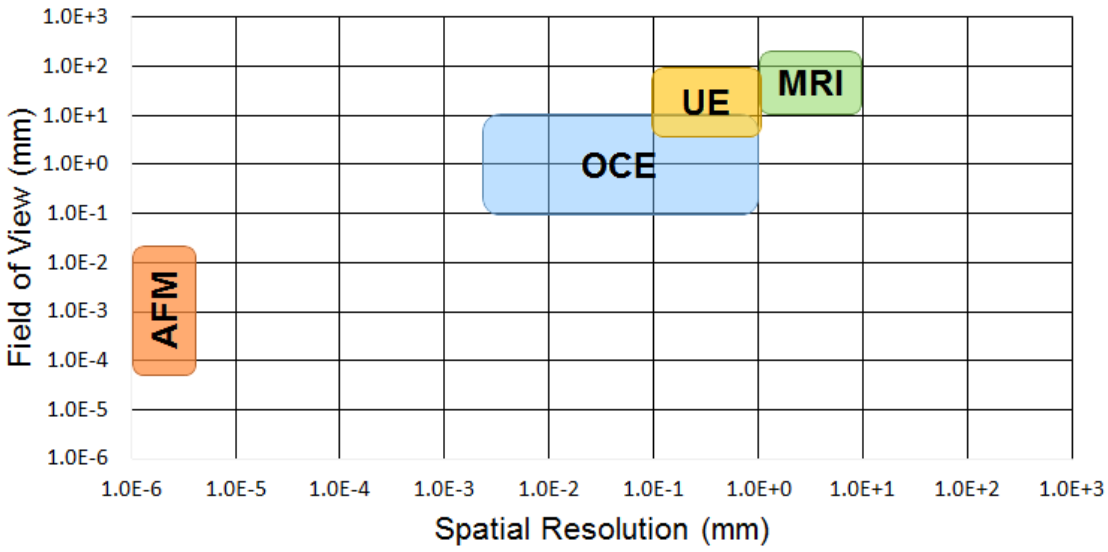

Figure 5. Spatial resolutions and fields of view of major elastography techniques.

Atomic Force Microscopy based Elastography

Alternatively, atomic force microscopy (AFM) based elastography methods can probe the mechanical properties at the level of a single cell by applying nano-scale indention (**Figure 5**) [104]. AFM as an elasticity method is capable of providing the contact force at the level of sub-nanoNewton to load the cell membrane and measure the induced deformations with sub-nanometer accuracy, making it the primary choice for studies in cell mechanics and cell biology [105]. For instance, high-resolution (1-5nm) AFM mapping of the mechanical heterogeneities allows the detection of cell pathologies [106]. However, AFM elastography has been mainly restricted to cellular mechanics studies due to the limited field of view and the measurement procedure [107].

Ultrasound Elastography

UE is the first of the elastography techniques developed to measure the mechanical properties of tissues and has been widely developed and used over the years for various clinical applications in various embodiments. In general, the UE techniques can be classified into a) strain imaging methods that use internal or external compression stimuli to provide a qualitative evaluation of Young's modulus, and b) shear wave imaging (SWI) that uses ultrasound-generated shear wave stimuli and provides shear wave speed, stiffness and/or Young's modulus.

Strain imaging can be further subdivided into: i) strain elastography that utilizes manual compression on tissues and is suitable for superficial organs such as breast and thyroid, and ii) Acoustic Radiation Force Impulse (ARFI) strain imaging in which the tissue excitation is based on internal physiologic motion (e.g.: cardiovascular or respiratory), and is therefore suitable for imaging deeper organs. The manually or physiologically applied stress is not quantifiable and thus a uniform normal stress is assumed to compute the Young's modulus. An alternative ARFI imaging method applies an external 'push' to

displace the tissue by using a high-frequency, short-duration acoustic pulse perpendicular to the tissue surface and then image and measure the displacement in a target region of interest. This imaging approach is implemented for example as Siemens Virtual Touch™ Imaging.

In contrast to strain imaging that measures physical tissue displacement parallel to the applied normal stress, SWI employs a dynamic stress to generate shear waves in the parallel or perpendicular dimensions. Measurement of the shear wave speed results provide qualitative and quantitative estimates of tissue elasticity. Currently there are three technical approaches for SWI: 1) 1-dimensional transient elastography (1D-TE), 2) point shear wave elastography (pSWE), and 3) 2-dimensional shear wave elastography (2D-SWE).

1D-TE utilizes a mechanical vibrating device to generate dynamic stress in the form of shear waves parallel to the excitation. The stiffness is estimated along an ultrasonic A-line in a fixed region that is selected by the ultrasound probe operator. Shear wave velocity is measured by the same probe and elasticity is calculated. This is the most widely used and validated technique for liver fibrosis assessment [108] and is commercially available as FibroScan™ (Echosens, Paris, France).

pSWE employs ARFI to generate a dynamic stress perpendicular to the tissue surface in a single focal location [109]. Shear waves are measured perpendicular to the excitation plane and converted to Young's modulus as a quantitative measure of tissue stiffness or elasticity. pSWE imaging can be performed on a conventional ultrasound machine using a standard ultrasound probe and can help the operator to visualize and select the region of interest using the B-mode. This provides an advantage over the 1D-TE in terms of direct visualization of the target tissue region. However, this method does not show a stiffness

image. Virtual Touch™ Quantification by Siemens and the Elast-PQ™ by Philips are the two commercially available pSWE systems on the market.

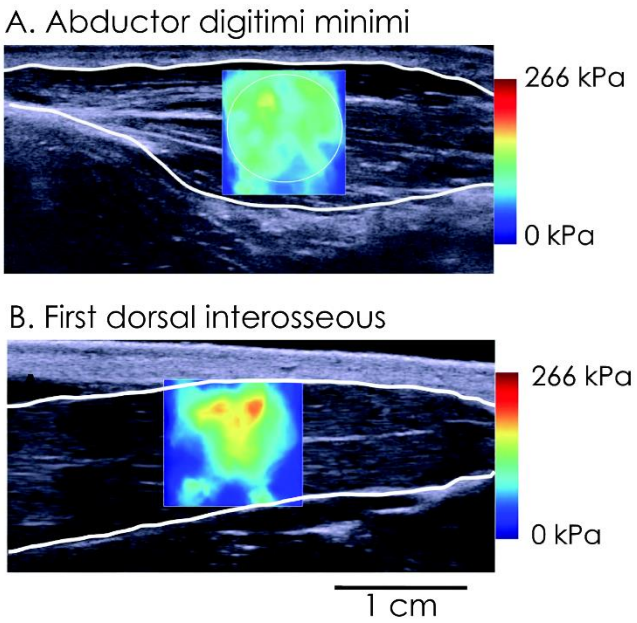

Figure 6. Supersonic shear imaging of the stiffness during contraction of the hand muscles abductor digiti minimi (A) and first dorsal interosseous (B). The scale is in kPa of shear modulus. (Reproduced from Bouillard et al., 2011)

2D-SWE employs ARFI to generate dynamic stress in the normal direction in multiple focal zones and shear waves are measured perpendicular to ARFI application. The rapid interrogation of multiple focal zones that is faster than the shear wave speed creates a near cylindrical shear wave cone that allows real-time monitoring of shear waves in 2D and results in generation of quantitative elastograms (**Figure 6**) [110]. This provides the operator with the advantage of both anatomical and color-coded tissue stiffness in real time. The following commercially available systems use 2D-SWE technology: Virtual Touch™Imaging Quantification by Siemens, Shear Wave™ Elastography by SuperSonic

Imagine, Shear Wave Elastography by Philips, Acoustic Structure Quantification™ by Toshiba, and 2D-SWE by GE Healthcare [111,112].

Ultrasound-based methods are of particular interest because of the various inherent advantages, such as wide availability including at the bedside and relatively low cost. However, just like MRE, limited spatial resolving ability of ultrasound imaging, and dependency on the signal-to-noise ratio measurement of the tissue displacement, restrict the spatial scales of UE at macroscopic level with the organ-size field of view and a typical resolution of hundreds of micrometers (**Figure 5**) [113,114]. Also, despite the wide availability of commercial UE systems, core assumptions such as the imaged tissue being linear, elastic, isotropic and incompressible, not only neglects the viscosity portion of the tissues but also complicates the comparison of shear wave speed measurements among different UE vendors that use different excitation frequencies [111,115].

Optical Coherence Elastography

OCE is at the forefront of optical elasticity imaging techniques and focuses on the micro-scale assessment of tissue biomechanics in 3D that is difficult to accomplish with traditional elastography methods. OCE is capable of providing real-time high resolution images of tissue elasticity (**Figure 7**) [116,117]. Research based on elastography with OCT or OCE has bloomed in the last decade [118–120]. As mentioned before, the first step of elastography is to mechanically load and excite the sample. A wide array of methods have been used to mechanically load the sample under test using OCE. Just like UE, the mechanical loading methods can be static or dynamic, contact or non-contact, localized or global, extrinsically applied or intrinsically present and its temporal profile can be quasi-static, harmonic or transient [119–125]. The method of measuring the sample displacement can be either speckle tracking or phase-sensitive detection, where the latter

has significantly improves imaging quality and sensitivity. The following section describes in some detail the wide range of specific implementations of the various loading methods.

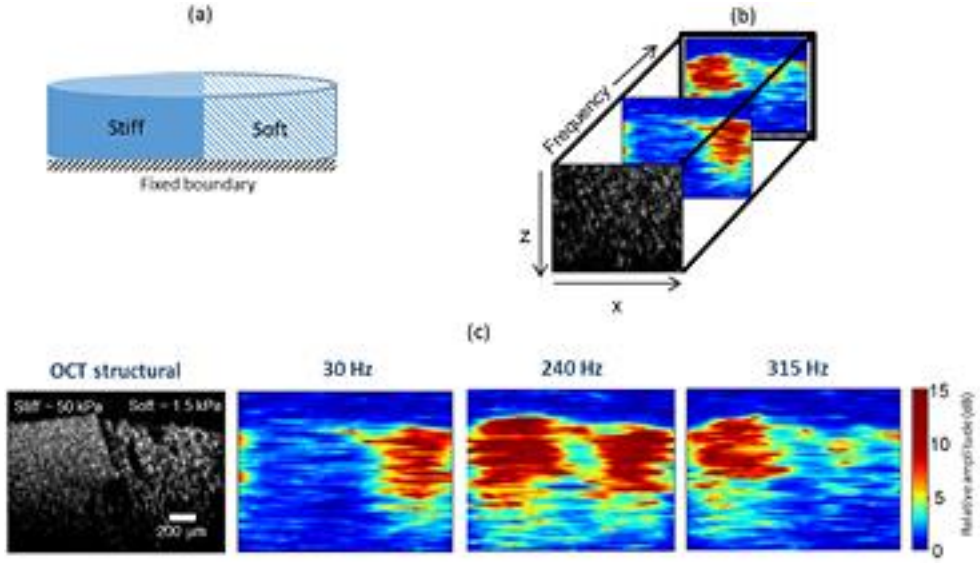

Figure 7. Spectroscopic MM-OCE in a heterogeneous side-by-side configuration phantom. (a) Geometrical model. (b) MM-OCE response at different excitation frequencies. (c) At lower frequencies (30 Hz) the soft region within the sample gives a higher magnetomotive response while at higher frequencies (315 Hz) the stiff region gives a higher magnetomotive signal. (Reproduced from Ahmad et al., 2015)

The first demonstration of OCE by Schmitt employed a static, global, planar compression that was induced by an annular piezoelectric actuator and window on the same side of the tissue as used for imaging [126]. The key requirement for such methods is the generation of comparable displacements across the field of view induced by a uniform application of stress across the sample that also results in a simple interpretation of the elastograms [127]. This is an issue for curved samples such as the eye or lumens of arteries. The issue in the eye has been resolved by using a curved gonioscopy lens has been used [128–130]. Indentation has been majorly used in the dynamic context as a point source of elastic

waves [91,131]. Local quasi-static indentation using a needle with a built-in OCT probe has been demonstrated to characterize tissue at depths well beyond the usual OCT penetration depth of a few millimeters in tissue [132,133].

Non-contact loading through use of ultrasound frequencies rapidly becomes problematic, due to the high attenuation of ultrasound in air, the high impedance mismatch between air and tissue, and the challenge of directly measuring the resulting tissue response in the megahertz range [121]. Ultrasound-based loading, to date, has almost exclusively been a contact method and has employed ARF, adopted from UE. ARF in OCE makes use of 10s μs-10 ms bursts of ultrasound in the megahertz range to modulate the stress induced in the tissue. The resulting displacement is detected as the axial displacement along the focused ultrasound beam [134–136] or shear wave associated axial displacement that is generated by the burst at some lateral offset from the focus [137,138]. It has also been shown that acoustic mechanical resonance can be detected along the axial direction by scanning the frequency of the amplitude modulation [139]. Shear wave propagation can be characterized with the ultrasound beam orthogonal to the OCT beam, a geometry suited to a few applications [140]. ARF can apply localized tissue displacements in the micrometer range at depths well beneath the surface of the tissue, an order of magnitude larger than the OCT resolution; making the ultrasound beam was almost uniform over the scanning region. Another benefit of ARF is that it could be integrated into catheter-based probes [141]. With technological advancement, such catheters may enable intravascular mechanical assessment of the arterial wall, a measurement currently only possible *ex vivo* [142]. However, ARF produces pressures that are large enough to be of safety concern for applications in the eye, which has led investigators to adopt a chirped-pulse radar method to reduce the peak ARF and numerically compress ultrasound induced shear waves post-detection into a short, localized high-pressure pulse [143]. Recent

technological innovations in piezo-ceramic materials enabled the realization of high-power ultrasound transducers capable of air-coupled ARF excitation in ex vivo porcine cornea [144,145], present intriguing possibilities for non-contact OCE.

Point dynamic loading has shown potential as a source of shear waves, and an attractive non-contact localized method is the micro-air puff developed and applied extensively by the Larin group [146,147], primarily to the cornea, but also to skin [148], cardiac and skeletal muscles [149], fat and soft tissue tumors [150], and kidneys [151]. An air puff excitation is similar to ARF in that it can deliver a localized and well-controlled impulse stimulus that can be followed by measurement of the tissue displacement or measurement of the air puff-induced elastic wave. A major benefit of the air puff is the possibility of using very small loading pressures (in the mPa range). However, this method is limited in how short the impulse can be, which confines the bandwidth of the elastic waves available for quantifying tissue viscoelasticity. Moreover, in contrast to ARF, it is limited to surface excitation, and cannot excite the sample internally.

Recently, elastic waves were induced by the Lorentz force generated from electrical current induced by an external alternating-current magnetic field flowing through the sample [152]. The inherent conductivity of biological tissues makes it possible to use this method for studying not only biomechanical properties, but also electrophysiological properties. A related alternative that was investigated by the Boppart group is the use of magnetic nanoparticles incorporated into tissues placed in an external magnetic field, to act as internal transducers for magnetomotive vibration [153,154]. The use of this method makes loading highly localized to individual or aggregations of nanoparticles that gets distributed throughout the tissue in the alternating-current magnetic field. The nanoparticles can be used to induce elastic waves [155] or to perform spectroscopic analysis by sweeping the excitation frequency and finding resonance modes for micro-

rheological analysis [153]. However, the adoption of this method has been limited due to challenges such as very small displacements that can be induced, and the requirements of a sufficiently high magnetic field gradient and relatively high concentrations of nanoparticle that make it difficult to maintain sufficiently low toxicity for *in vivo* applications.

Resonance based OCE techniques have also been reported to quantitatively assess biological tissues [139,154]. Empirical models, such as the Kelvin-Voigt and Maxwell models, have been widely used to describe the viscoelastic behavior of biological tissues [156]. Taking the Kelvin-Voigt body as a base, a biological tissue can be modelled as a parallel combination of a linear spring and a dashpot that are representing the elastic and the viscous properties of the tissue sample, respectively. For an underdamped harmonic oscillator, the material stiffness is known to be directly proportional to the square of its natural frequency. In OCE, several loading functions, including the step function [135,153], the sine or cosine function [157] and the square pulse [158], have been used for creating damped oscillations in the sample. Approaches such as applying fast Fourier transform [158] and performing least-square regression [153] have been utilized in OCE to obtain the frequency information from the captured temporal dynamics of the sample.

When modelling a biological tissue using the Kelvin-Voigt model, it is assumed that the constant stress applied to the tissue produces constant strain in the spring and constant strain rate in the dashpot [156]. Although a simple empirical model can be utilized for basic description of tissue's mechanical characteristics, more adaptive models employing finite element analysis [159] could provide more accurate representation of the tissue and reduce errors in the quantitative assessment of the tissue elasticity using OCE [135]. The assumption of identical or negligible viscosity of the test sample could create artifacts for the qualitative OCE imaging methods that utilize natural frequency as the mechanical contrast. To date, the OCE techniques based on resonance have been clinically used to

either differentiate the tissue types [160] based on the difference of their resonance frequencies or used the resonant frequencies to estimate the elasticity modulus [154]. However, no calibration studies have been performed to compare the moduli computed from the resonance based techniques to other state-of-the-art biomechanical testing systems. Commercial devices like Buzz-o-sonic (BuzzMac International, WI, USA) that are based on the concept of impulse excitation technique are available in the market. These devices utilize a small impulse tool to vibrate an elastic solid in flexure mode such in order to determine its resonant frequency, much akin to a tuning fork. The also compute the viscoelastic properties of the material using half-power bandwidth methods. However, these devices cannot be used to compute the viscoelastic properties of a soft tissue.

In addition to the direct employment of natural frequency as an indicator, the resonance phenomenon has been utilized to create mechanical contrast by detecting strain- or displacement-related parameters during the sweep of the loading frequency [139,161,162]. Resonance occurs when the external driving frequency equals the natural frequency of the tissue, causing increased displacement amplitude or strain. Since tissue with varying stiffness appears to have distinct natural frequencies, the spatial mapping of the vibration spectrum obtained from resonance based OCE can be plotted as an elastogram [161,162]. Alternatively, the natural frequency of the tissue can also be estimated through the frequency-sweeping stimulation [139], thus enabling quantitative measurement of the tissue elasticity [154]. While the OCE techniques based on tissue resonance rely on the same assumptions as the approaches that make direct use of natural frequency, relatively more thorough tissue characterization is available over a broad spectral range [162]. However, this approach requires processing larger amount of hyperspectral data.

The specific characteristics of tissue response to the static or dynamic loading determine the parameters for measurement. The relationship between these parameters and tissue's biomechanical properties (e.g. elastic modulus) generates the mechanical contrast in OCE. Several OCE techniques have been reported for applications in tissue characterization of skin, soft-tissue tumor, arterial walls, muscle, cornea and airway wall [19,163–167]. However, the unknown distribution of the stress through the sample prevents direct quantification of the Young's modulus, which significantly limits the application of OCE techniques employing displacement amplitude or strain methods for accurate biomechanical comparison across samples. Also, the potential non-uniform distribution of the stress could lead to artefacts in the elastography results. The ability of SWE to quantify tissue's Young's modulus highly relies on the assumptions made to the mechanical performance of the tissue such as the negligible viscosity of the tissue. Additionally, the values for tissue moduli reported in many studies are in the kPa range [127] as opposed to the MPa range that is expected for biological tissues and polymers [13,168]. The primary reasons for this discrepancy may be the assumption of uniform stress or other assumptions made about the tissue's mechanical nature (e.g. linear, elastic, homogenous, isotropic) in order to compute elasticity modulus from displacement strain or SWE-based methods. The fact that most of the biological tissues are viscoelastic makes it a challenge for many of these methods to accurately determine the mechanical properties of the tissues as the viscosity component of these tissues has not yet been widely studied. Issues like the impact of stress on mechanical contrast and the reporting of strain when reporting an elastic modulus, have afflicted both UE and OCE and is still an area to be explored [120].

The ability to characterize tissues and implant materials by measuring the natural frequency when a vibration is applied to a substrate is very useful for evaluating tissue

pathology or implant properties. In fact, several diseases such as Osteogenesis Imperfecta [169] and tumor differentiation [170] are characterized by changes in the mechanical properties such as modulus and hardness. However, it is important to be able to accurately calculate the value of the modulus since the modulus depends on the exact composition of the macromolecular components, their orientation and the degree of crosslinking of the components [45]. Thus, it will be of a great clinical impact to develop a OCE technique to measure the viscoelastic properties of soft tissues that can be successfully correlated to the measures obtained from other state-of-the-art techniques for biomechanical testing.

Placenta

The placenta, the key interface between the mother and the fetus, is critical for growth and survival of the developing fetus. Placental shape and vasculature have been identified to differentiate normal and high-risk autism population [171]. Placental histology is widely used to diagnose placental abnormalities like intra-uterine growth restriction or acute and chronic inflammations [172]. Villus immaturity and chronic fetal hypoxia are common in diabetic placentas, resulting in a lower fetal/placental weight ratio as compared to normal placentas [173]. Although the basic components (e.g. collagen) and their orientations for different layers of the placenta at progressing gestational ages are known [174–177]; the normal and pathological ranges of placental biomechanical properties remain largely unknown. Despite the extensive use of ultrasound and Doppler imaging in obstetrics and gynecology, the biomechanical properties of the placenta have been sparsely studied. Shear wave elastography has been recently used to study differences in shear wave speeds between perfused post-delivery normal placentas and placentas injected with vasoconstrictors and vasodilators and any gross pathologies [178]. However, the study was limited to differentiating the normal and growth-restricted placentas in terms of just

the difference in the shear wave velocities and the stiffness computed from them. Placenta is a large organ that is complex right from its microscopic to macroscopic structures. Given its environment, and anatomical and functional changes over gestation, it is imperative to study the factors influencing the placenta as they can have great impacts on the developing fetus and later on the infant wellbeing. Chorionic plates contain the fetal vasculature and form the base for terminal villi. This fetal vasculature is crucial in blood, nutrient and oxygen transport between the mother and the fetus. Simpler methods can be used to assess the biomechanical properties of the chorionic plates of the placentas. A stiffer or a more compliant matrix of the chorionic plate can alter the developing fetal surface vasculature of the placenta and may eventually aid or hinder the fetus from achieving its optimal growth. If a clinical ground truth is established about the difference in the biomechanical properties of chorionic plate tissues from normal and diseased placentas, it may provide a path to an early diagnostic tool for adverse placental conditions using UE or MRE.

This goal of this dissertation is to develop and validate a nondestructive biomechanical testing method to measure the viscoelastic properties of biological tissues. It will also study the moduli of early term, normal and pathologic placental chorionic plates.

CHAPTER 2: DEVELOPMENT OF VIBRATIONAL OCT SETUP AND MEASURING ELASTIC MODULUS OF MONO- AND MULTIPHASIC BIOLOGICAL TISSUES

Note: Portions of this chapter have been published in the following citations and represent the original work of the candidate:

1. Shah, R., Pierce, M. C., & Silver, F. H. (2017). A method for nondestructive mechanical testing of tissues and implants. Journal of Biomedical Materials Research Part A, 105(1), 15-22.
2. Shah, R. G., Pierce, M. C., & Silver, F. H. (2017). Morphomechanics of dermis-a method for non-destructive testing of collagenous tissues. Skin Research and Technology, 23(3), 399-406.
3. Shah, R. G., DeVore, D., Pierce, M. C., & Silver, F. H. (2017). Vibrational analysis of implants and tissues: Calibration and mechanical spectroscopy of multi-component materials. Journal of Biomedical Materials Research Part A, 105(6), 1666-1671.

Specific Aim 1

Develop and validate the efficacy of vibrational OCT system to measure Elastic modulus of mono- and multi-phasic biological tissues.

Hypothesis and Rationale

Elastography techniques including UE, MRE and OCE have been widely adopted for imaging and characterizing tissue microstructures in several pre-clinical applications [86,89,94,118]. The Kelvin-Voigt models assumed to characterize the tissues using these techniques have shown that material exhibits almost purely elastic response when it is vibrated at its natural frequency [119,179]. Thus, the resonant frequency of a material is

related to its elastic modulus [180]. The resonant frequency of the samples and their physical dimensions will be used to determine their elastic moduli using a benchtop setup. The central hypothesis of this aim is that the vibrational technique modulus obtained from the material's resonant frequency will be similar to that found using uniaxial tensile testing. Multiphasic samples will exhibit multiple resonant peaks. These moduli will be compared to those obtained using the gold standard method of uniaxial tensile testing and a calibration curve will be generated.

Experimental Methods

Sample preparation

The samples used for the experiments in this thesis included human decellularized dermis, chemically treated and untreated human dermis, silicone rubber, pig skin and bovine cartilage. All samples except silicone were soaked in phosphate buffer solution at pH 7.4 for at least 30 minutes before being tested wet at 22^{o}C.

Silicone rubber sheets were produced by mixing polydimethylsiloxane base material with a curing agent and allowing the mixture to harden in a 100 mm diameter petri dish. Polydimethylsiloxane (PDMS, silicone) samples were fabricated from a 2-part kit (Corning Sylgard-184) by mixing silicone base and curing agent in varying proportions, relative to the standard ratio of 10:1. Samples with a cross-sectional area of about 0.8 cm^2 were cut to an initial length (6 cm) and width (2 cm).

Decellularized human dermis was obtained from the tissue as described previously [18]. Additional decellularized human skin samples were treated with carbonate/dicarbonate buffer and glutaric anhydride to alter the charge density of collagen. Three sets of decellularized dermal samples were tested in this study: 1) decellularized dermis (dermis), 2) carbonate/dicarbonate controls (control dermis), and 3) glutaric anhydride treated

dermis (treated dermis).

Three samples of depilated pigskin, with a thickness of ~2 mm, composed of epidermis and dermis, were obtained at slaughter from Spear Products (Coopersburg, PA) and stored at 4^{o}C. Three bovine femoral cartilage and subchondral bone samples with a thickness of approximately 1mm were obtained from Spear Products (Coopersburg, PA) and stored at -4^{o}C until it was tested. Samples were thawed and soaked in phosphate buffer at pH 7.4 for at least 30 minutes before testing at 22^{o}C. Cartilage was removed from the subchondral bone by mechanical scraping using a surgical blade to evaluate the mechanical properties. The length, width and depth of all the samples were measured using digital calipers and the weight was measured using an electronic scale.

OCT system setup and Vibrational testing

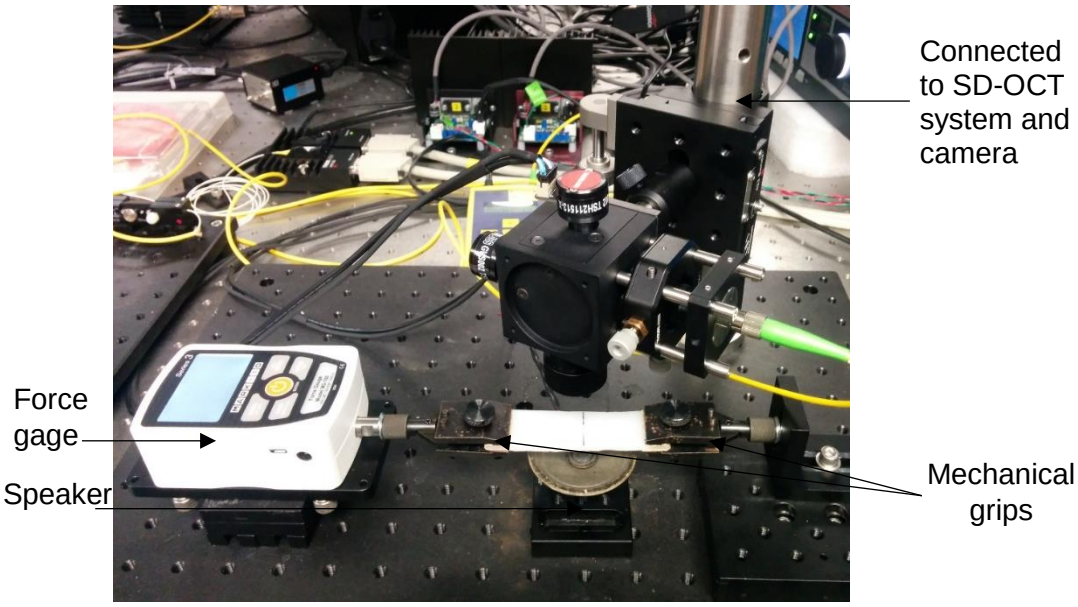

Figure 8. Vibrational OCT testing benchtop setup

A benchtop spectral-domain optical coherence tomography (SD-OCT) system with an external speaker was set up to vibrate clamped samples at different strains (**Figure *8***). Transverse forces were applied to the sample by positioning an acoustic loudspeaker

(Intervox S225RA-40) beneath the sample. A function generator (Agilent) was used to drive the speaker with sinusoidal waveforms at varying amplitude and frequencies in the preliminary experiments. Later, the LabVIEW block diagram and Matlab scripts were altered to 1) drive the speaker from the computer using the National Instruments data acquisition device USB 6001; 2) step vibrational frequency every 10 seconds based on user-selected starting and ending frequencies, and step size; and 3) capture a B-scan 5 seconds after the speaker is vibrating at the current step of frequency.

SD-OCT system (**Figure 9**) measured the transverse sample displacement. This system used a fiber-coupled superluminescent diode light source with 1325 nm center wavelength and 100 nm bandwidth (full-width at half maximum). The source is connected to a fiber-optic circulator that directs light to a fiber-optic splitter, sending 90% of the source light to the sample and 10% to the reference arm. The sample arm contains a 60 mm focal length lens to focus light into the sample. The reference arm contains a variable neutral density filter to adjust the reference light intensity and a stationary mirror. Light returning from the sample and reference arms is recombined at the splitter and directed to a spectrometer for detection. The spectrometer comprises a 50 mm collimating lens, an 1145 lines / mm diffraction grating, and a 100 mm focal length lens to focus the spectrally dispersed light onto a 1024 pixel InGaAs line-scan camera (UTC Aerospace Systems, NC, USA). The measurements of signal intensity as a function of optical wavelength ($I(\lambda)$) using the spectrometer's previously established pixel-to-wavelength calibration. Data was transferred to a PC via a CameraLink frame grabber board (National Instruments, TX, USA). All data acquisition and storage was controlled by in-house developed LabVIEW software.

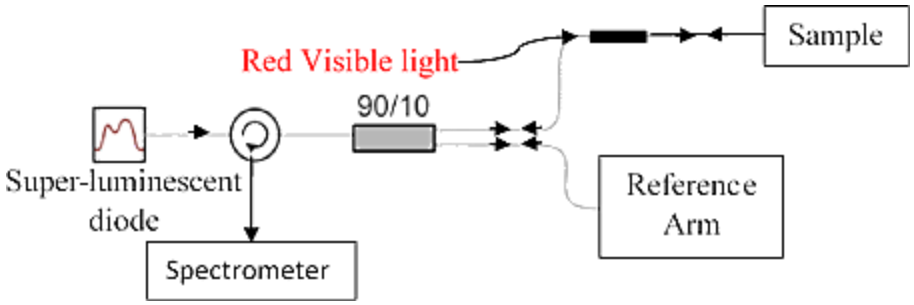

Figure 9. Spectral-domain OCT system schematic

The OCT sample arm beam was directed to a single location on the sample to measure transverse sample displacement as a function of time. 4000 spectral interferograms ($I(\lambda)$) were acquired at a sampling frequency of fs = 28.8 kHz. After using the relation $k = 2\pi/\lambda$ to convert each measured interferogram $I(\lambda)$ from a function of wavelength to a function of wavenumber I(k), Fourier transformation of the I(k) signal yielded the magnitude (I(z)) and phase ($\Delta\phi(z)$) of the backscattered signal returning from each depth location (z) within the sample.

The sample displacement can be measured using either the amplitude of the OCT signal or the phase. All the displacements in this thesis were computed using the phase information as most of the samples undergo minor displacement in the range of a few micrometers that are better detected using the phase information rather than the amplitude of the OCT signal. As the sample undergoes time-dependent deflection due to the external driving force, the measured phase was extracted from the location of the sample surface. This phase value grows until it reaches $+\pi$ (180°) or $-\pi$ (-180°), depending on the direction of sample displacement. Further displacement beyond $\pm\pi$ results in "wrapping" of the phase (**Figure 10a)**, as evidenced by a jump of exactly 2π (360°) in the calculated value.

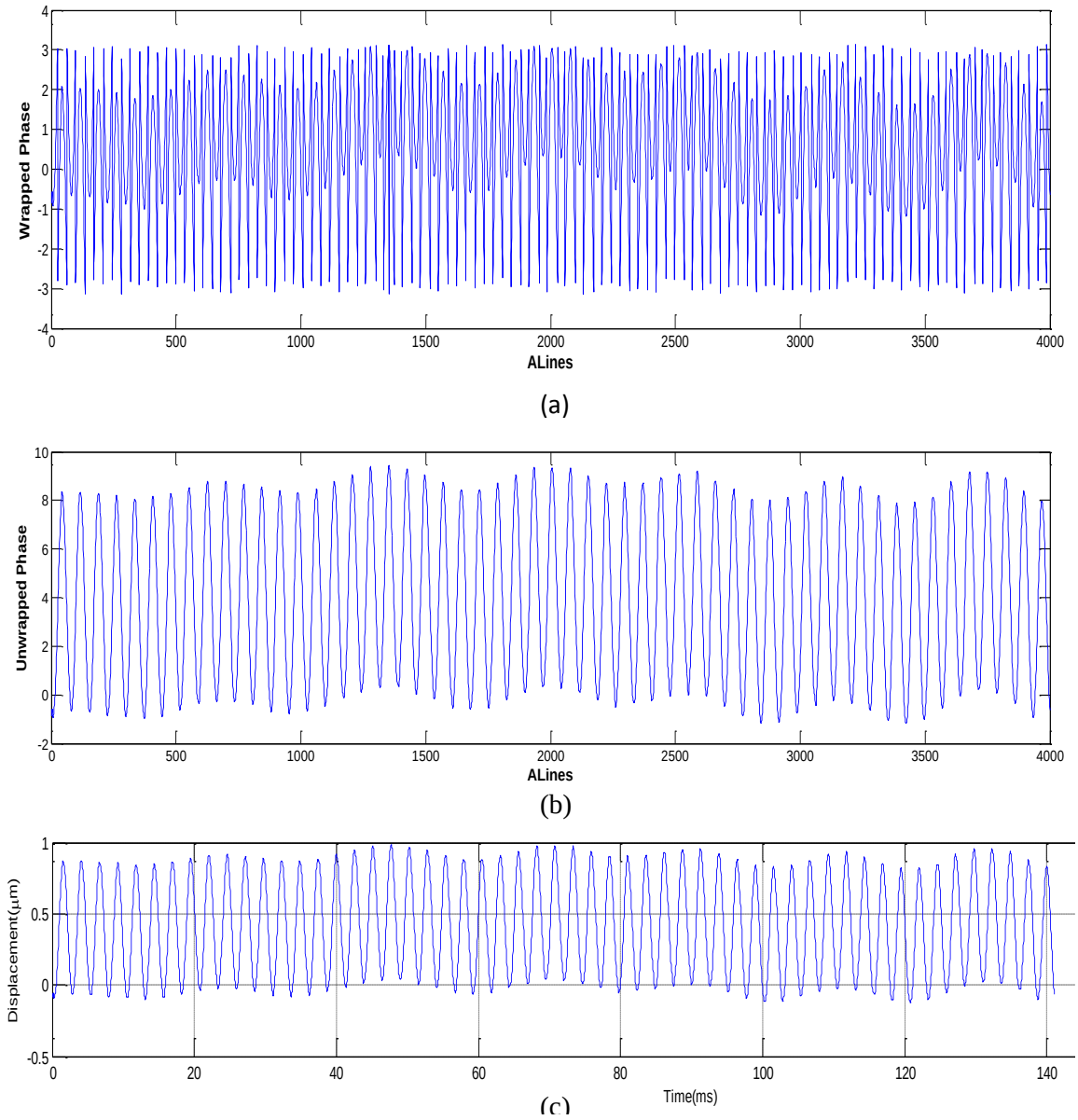

Figure 10. Processing raw OCT data. (a) An example of the wrapped phase information of a wet dermis sample at a given frequency. The values fluctuate between ±π (b) The wrapped information in (a) is unwrapped to correct the displacement beyond ±π. (c) The unwrapped information in (b) is converted to actual displacement using the wavelength information. (Note: the slow oscillation in Figures (b) and (c) is the result of the 50Hz electric noise that was eliminated using digital filters in the data processing steps)

The measured phase $\Delta\phi$ at the sample surface was therefore corrected for phase wrapping ("unwrapped", **Figure 10b**) and converted to physical displacement Δz using the relationship $\Delta z = (\lambda_0/4\pi)\Delta\phi$ (**Figure 10c**). All data processing was performed on a PC using standard algorithms written in custom developed Matlab 2014 software (MathWorks, MA, USA).

As described above, sample displacement (Δz) was measured as a function of time (t) based upon 4000 discrete measurements obtained at a sampling frequency of 28.8 kHz. Fourier transformation of the measured $\Delta z(t)$ data allows the frequency response (power spectrum) of the sample to be examined. In our experimental setup, the Nyquist frequency limit is 14.4 kHz and the resolution in frequency space is 7.2 Hz. The ability of our SD-OCT system to accurately measure a sample's vibration frequency was evaluated by the measured peak displacement frequency to the loudspeaker driving frequency set at the function generator.

The displacement data was digitally filtered using a third order Butterworth bandwidth filter with a lower frequency threshold of 60 Hz and an upper frequency threshold of 1050 Hz. The lower threshold of 60Hz was selected to eliminate the electrical noise at 50Hz. For input frequencies less than 60 Hz, a low pass filter was used with a threshold of 100Hz. The filtered sample displacement at each frequency was plotted versus time as seen in **Figure 10c**.The mean peak-to-peak amplitude of the filtered displacement output was used to obtain the sample displacement. The resonant frequency of each sample was initially estimated by measuring the transverse displacement resulting from sinusoidal driving frequencies ranging from 50 Hz to 1000 Hz, in steps of 50 Hz. Once the region where the maximum frequency lies was identified, smaller steps of 10 Hz were used to more accurately identify the peak frequency and the actual resonant frequency. At each driving frequency, the value of the sample displacement at that frequency was recorded,

representing the “raw” frequency response for the sample. The driving speaker has its own frequency response (**Figure 11**) that needs to be calibrated. In order to correct for the frequency response of the driving speaker itself, the raw sample frequency response was divided by the frequency response of the speaker, independently measured by SD-OCT to obtain a weighted displacement of the sample under test. The resonant frequency of the sample was then identified from the peak of the corrected frequency response plot.

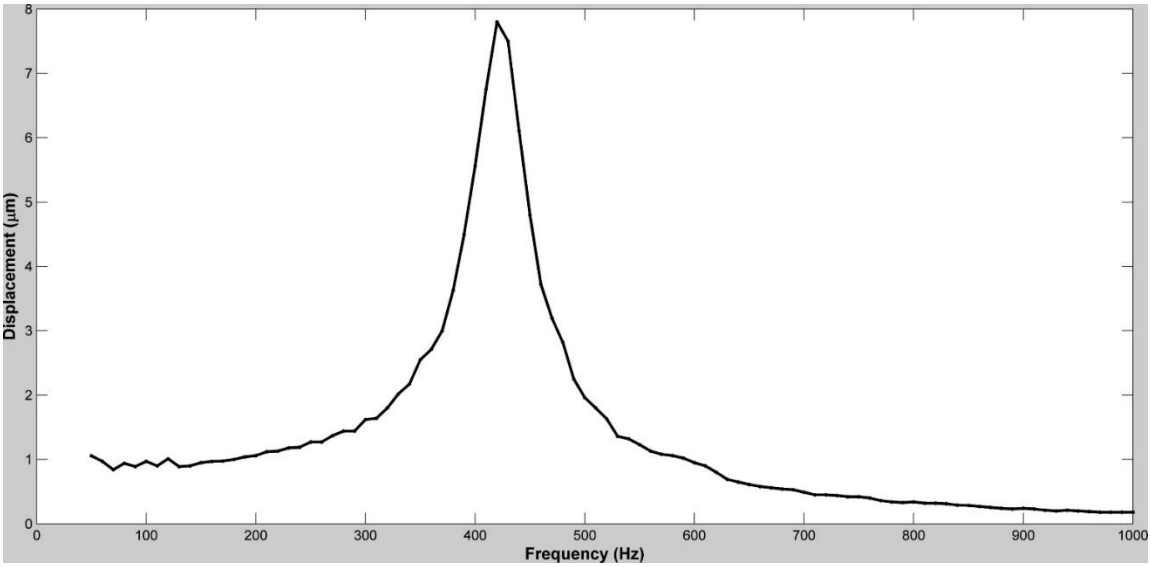

Figure 11. Frequency response of the Intervox speaker used for in vitro studies. The speaker resonates around 420 Hz.

When a low-frequency (<5kHz) external excitation is applied to a thin isotropic solid, elastic waves of different types are generated on its surface and volume [179]. This study involved applying an oscillating mechanical vibration in the form of externally applied sound waves to a sample and identifying its natural frequency. The wave velocity is the velocity with which planes of equal phase progress through the sample. Equation (1) shows the relation between the longitudinal wave velocity of a vibrated object and its natural frequency, and equation (2) demonstrates the relationship between the elastic modulus and the wave

velocity of the object [179,180].

$$V = \omega_n \lambda \qquad (1)$$

Where, $\omega_n = 2\pi f_n$ and the harmonic wavelength, λ, is related to the sample length L [181]. ω_n and f_n are the natural frequency in rad/s and Hz, respectively; L is the sample length in m, and V is the longitudinal wave velocity in m/s

$$E = \rho V^2 \qquad (2)$$

Where E is the elastic modulus in Pa, ρ is the material density in kg/m^3,

It must be noted that the above equation holds for an infinite elastic solid homogenous object that is clamped at both ends and is vibrated in between the two ends. Also, the relationship with the elastic modulus holds true for objects with a length to width aspect ratio of at least 4:1, and where the depth of the testing sample is negligible as compared to the length and the width. The negligible thickness of the test sample justifies neglecting the shear in transverse direction. If the sample to be tested is thicker, than the sample is considered to be a bulk solid. In which case the transverse shear needs to be considered and the bulk modulus comes into picture, increasing the value of the elastic modulus [179]. All the samples used in this dissertation had a length: width aspect ratios of > 4:1 and had thicknesses that were significantly smaller than the other dimensions. Also, even though biological tissues are nonlinear, they behave linearly for smaller strains such as the ones used in this study; thereby justifying the use of equation (2).

The relationship between the elastic modulus of the material and its natural frequency can be approximated from the above two equations as follows:

$$E = M(2\pi f_n)^2 L/A \qquad (3)$$

Where M is the object mass in kg, A is the cross-sectional area in sq.m and L is sample

length in m. This relationship between the elastic modulus of a material and its natural frequency is similar to that established in the literature [180–182]. Again, even though it is well established that the elastic modulus is proportional to the square of the resonant frequency and the material density, the proportionality constant will change depending on relative dimensions of the test sample, mode of vibration, method of clamping the test sample, material composition, properties and geometry of the test sample.

Uniaxial Tensile Testing

Samples were mounted in 1” wide grips with one end held stationary on a manual translation stage (Thorlabs, NJ, USA). The other end of the sample was attached to a force gage (Mark-10, NY, USA) in a standard tensile test configuration. Each sample was tested in uniaxial tension at 22^{o}C by adding strain increments after each force measurement was made. Varying axial deformations between 1 and 20% were applied through adjustment of a graduated translation stage. The resulting axial force (F) was measured by the force gage and recorded for subsequent calculations.

For Poisson’s ratio computation, the samples were imaged from a fixed height using a standard point and shoot camera at each step of the loading stage. The images were then read in Matlab 2013 (MathWorks, MA, USA) to measure the changes in lateral dimension at each step and compare them from the starting position to compute the lateral strain. The longitudinal strain was computed by the changes in the loading of the manual translation stage in the longitudinal direction. The Poisson’s ratio of the sample was computed at each step as the ratio of the transverse strain to the axial strain.

Effect of Strain on Resonant Frequency

The decellularized human dermis and silicone samples were stretched at different strains and their resonant frequencies were computed for each run of each strain. In addition, the moduli were computed for the vibrational OCT tests and compared to the moduli from the

uniaxial tensile tests.

Chemical Testing and Calibration Curve

A calibration curve was plotted by comparing the uniaxial tensile moduli and vibrational testing moduli of a variety of samples made from silicone rubber, decellularized human dermis, and modified decellularized dermis to prove the efficacy of the vibrational OCT method in computing the elastic modulus of a material. The strain on the samples ranged from 1-14% for tensile measurements and 5-14% for vibrational studies.

Preliminary *in-vivo* testing

In vivo studies on the mechanical properties of skin and healed scar tissue on the human arm were conducted by using a 24 mm x 14 mm rectangular speaker (Digi-Key, Thief River Falls, MN) that was taped to the skin using surgical tape and hardwired to a Samsung cell phone. A frequency generating cellphone app capable of driving the speaker between 10Hz and 20kHz was used to generate sinusoidal sound waves that vibrated the skin. The speaker was calibrated by determining its frequency response in the frequency range of 50 to 1000Hz. The sound intensity was low enough to be undetected unless the speaker was placed close to the subject's ear. The speaker was located about 2.5 cm from the beam location and did not interfere with impingement of the light on the skin. The location of the incident beam on the skin influenced the extent of skin displacement but not the measured resonant frequency. The signal generated by vibrating the skin with the Digi-Key speaker was processed in the same manner as that for *in vitro* studies. The subject's arm was placed in a resting state on an insulated steady surface to reduce the false signals from electrical noise and subject movements. Multiple scans were taken for each frequency to reduce the artifacts arising from the subject's movements and the scans were only taken when the imaged surface was at a pre-marked location on the live OCT image. Digital band-pass filters were used during the processing of OCT signals to

eliminate the artifacts at low-frequency range that includes electrical noise and most of the subject movements.

For elastic modulus computation, the density of the normal skin and scar tissue was assumed to be same as that of decellularized dermis samples from previous studies [58,183]. Based on the previously performed calibration study [58] and equation (3), an equation derived from the relationship between the material density, resonant frequency, and elastic modulus of the material was used to compute the in vivo moduli for normal skin and scar tissue. The results of studies reported for strain versus modulus of decellularized dermis from [58] were used to back-calculate the strain of normal skin and scar tissue in vivo.

Results and Discussion

Chemical study and Calibration curve computation:

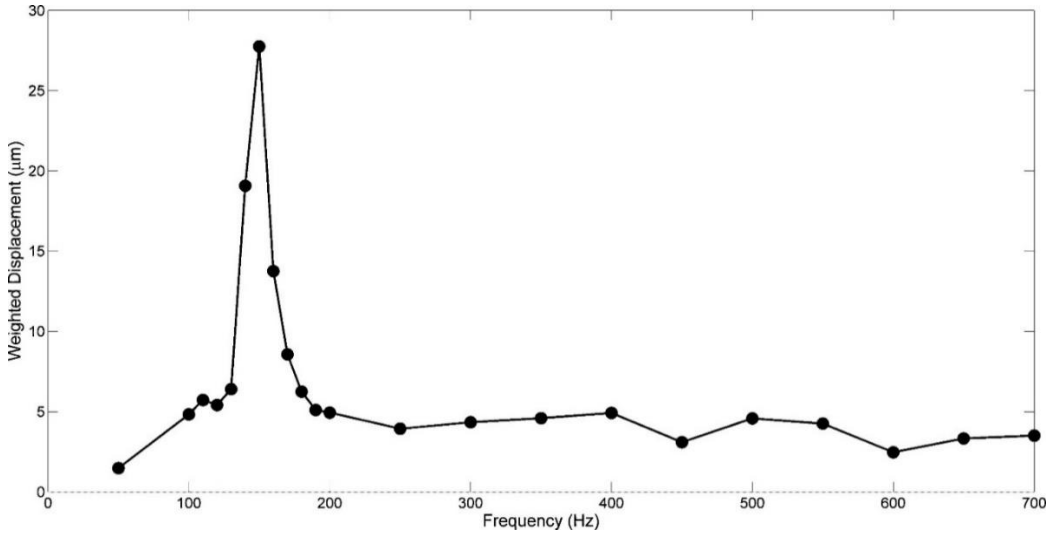

Figure 12. Plot of weighted displacement versus frequency, determined from vibrational OCT for decellularized human dermis. Dermis was placed under tension at 5% strain and its resonant frequency was determined from its maximum displacement caused by the sinusoidal vibrational waves. The modulus was calculated from the resonant frequency using equation (3)

A variety of samples made from silicone rubber, decellularized human dermis, and modified decellularized dermis were tested both in uniaxial tension and using vibrational analysis. **Table 1** gives a summary of the samples studied and the strains used to develop the calibration curves.

Table 1. List of samples tested to generate the calibration curve

Sample	**Number**	**Strains**
Decellularized dermis	3	5%, 10%, 12%, 14%
Control Dermis (Carbonate treated)	5	5%, 10%, 11%, 12%, 13%
Treated Dermis (Glutaric anhydride treated)	7	10%, 11%, 12%
Silicone	2	12%

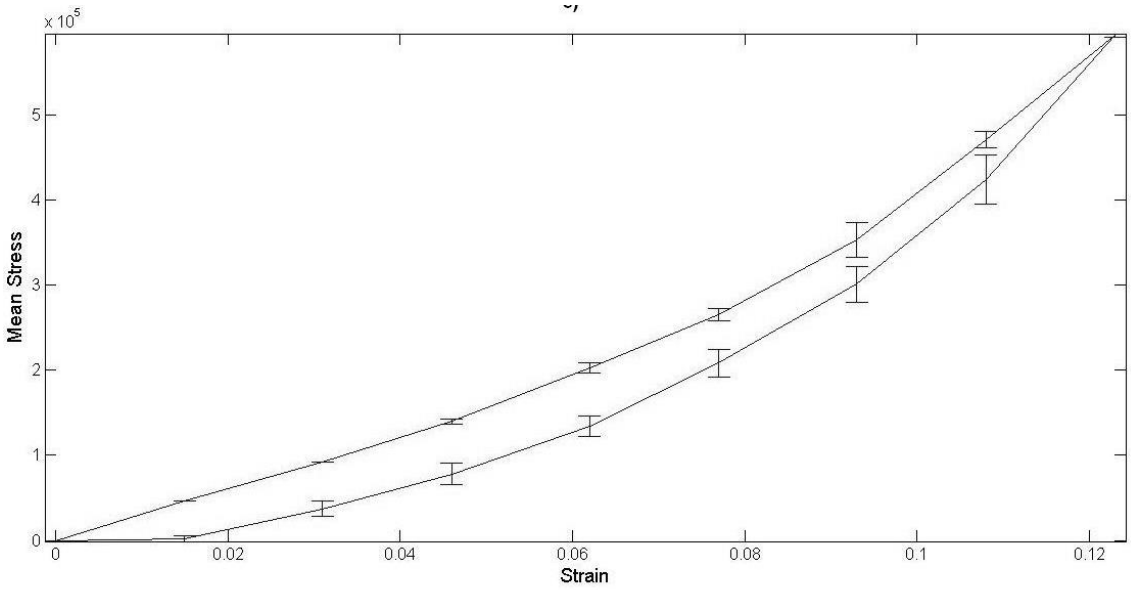

Figure 13. Mean stress-strain curves for wet decellularized human dermis as measured from force-extension curves. The loading curve is above the unloading curve and after a rest interval the stress and strain returned to (0, 0). The error bars represent the standard deviations of the stress measures obtained during the multiple runs of uniaxial tensile testing of the decellularized human dermis sample.

A typical plot of weighted displacement versus frequency for decellularized dermis is shown in **Figure 12**. The natural frequency of each material was obtained from such plots and its modulus for the vibrational study was calculated using equation (3). All the tensile testing moduli were calculated from the slopes of the tensile loading plots as illustrated in **Figure 13** that shows a tensile loading-unloading plot for a wet dermis sample.

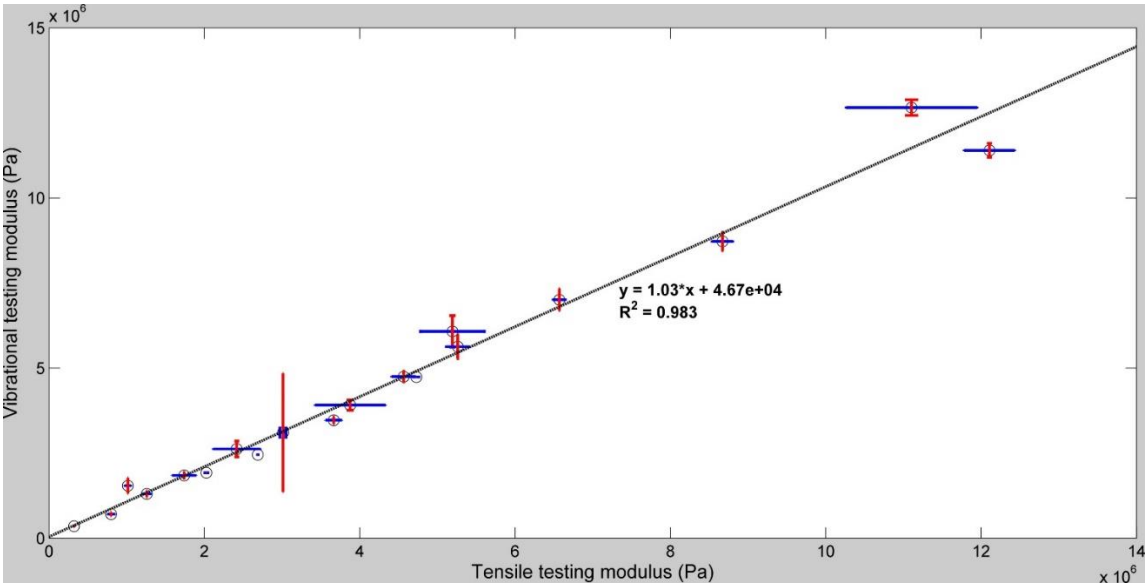

Figure 14. Calibration curve of the modulus determined from vibrational measurements, versus the modulus determined from the slope of tensile stress-strain measurement for decellularized dermis and silicone rubber, cycled in tension at strains between 5 and 14%. The calibration curve was prepared using data obtained from vibrational (Figure 10) and tensile measurements (Figure 13) for samples stretched up to three tensile cycles. The horizontal and the vertical error bars represent the standard deviations of the moduli measured during the multiple runs of each sample using the uniaxial tensile testing and the vibrational OCT methods respectively.

Figure 14 shows a plot of the modulus calculated from vibrational studies (E_v) versus the modulus determined by tensile testing (E_t), for all samples tested for strains between 1 and 14%. The equation for the linear least-squares fit line shown in **Figure 14** is:

$$E_v = 1.026\ E_t + 0.046 \qquad (4)$$

Where the correlation coefficient for the line is 0.984 and moduli are in Pa. The relationship between moduli determined using vibrational and tensile measurements is approximately linear and has a small Y intercept, suggesting that moduli measured using the vibrational technique provide a good estimate of the values obtained using tensile testing for strains up to 14%. OCT and vibrational analysis help in computing moduli of ECMs containing collagen fibers by determination of the resonant frequency. Measured resonant frequencies for decellularized dermis and silicone rubber, when converted into moduli, correlate well with the tensile moduli measured for the same samples.

Table 2. Moduli for control and treated human dermis measured using tensile testing and vibrational analysis. '±' indicate the standard deviations of the measurements. Note: * indicates no standard deviation was observed but the standard error for resonant frequency measurements was ±5 as the input frequencies were varied in steps of 10.

Sample	Sample Thickness (mm)	Strain (%)	Tensile testing modulus (MPa)	Vibrational testing modulus (MPa)	Resonant Frequency (Hz)
Dermis	0.93	5	2.69 ± 0.021	2.46*	150*
		14	6.57 ± 0.079	7.01 ± 0.32	253.33 ± 5.77
Control Dermis	0.92	5	3.01 ± 0.039	3.11 ± 0.142	306.67 ± 5.77
		12	4.73 ± 0.051	4.74*	340*
Treated Dermis	1.5	5	0.67 ± 0.037	0.71 ± 0.052	156.67 ± 5.77
		12	0.94 ± 0.098	0.97 ± 0.062	183.33 ± 5.77

When decellularized dermis was treated with glutaric anhydride, a chemical that reacts with free primary amino acid residues on collagen and alters the charge density, its mechanical behavior changed as shown in **Figure 15**. After treatment with glutaric anhydride the tensile and vibrational moduli of decellularized dermis decrease as shown

in **Table 2**. The stiffness decrease is associated with an increased swelling and thickness of the dermis as shown in **Table 2.**

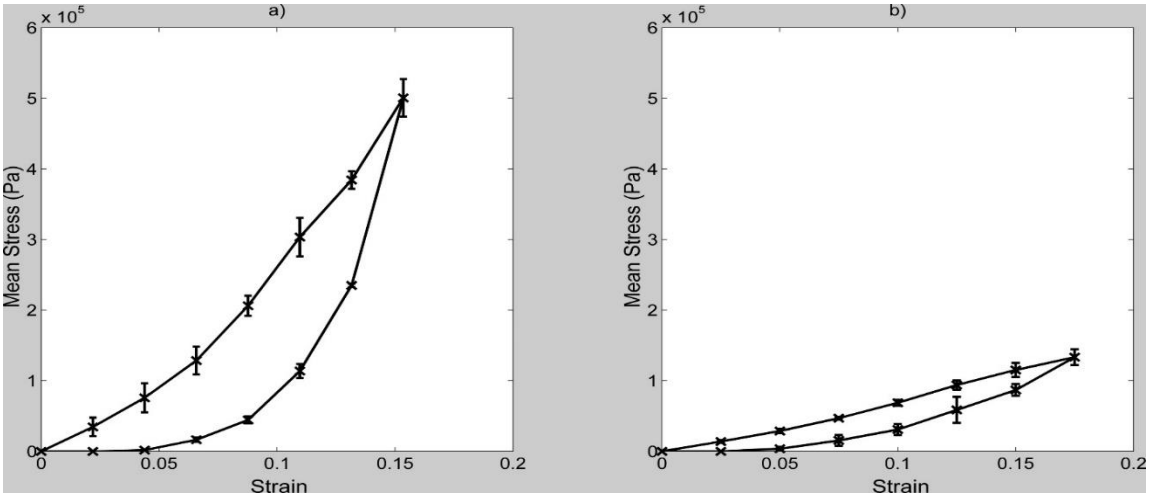

Figure 15. Stress-strain curves for (a) control human dermis and (b) glutaric anhydride treated dermis. Note the modulus (tangent to the stress-strain curve) decreases in the treated dermis due to swelling of the sample. The error bars represent the standard deviations of the stress measurements obtained during the various runs of uniaxial tensile testing of the sample.

There has been considerable interest in the cosmetic, plastic and maxillofacial surgery in identifying methods to rejuvenate and promote healing of aged and repaired skin. While many of the cosmetic and injectable treatments give the appearance of altering skin mechanics or at least to cause wrinkles to be less obvious, treatments are needed that actually modify the ECM. The results suggest that skin mechanics can be modified by altering the physicochemical properties of the collagen fibers by changing the charged amino acid residues. In addition, using vibrational analysis, these changes can be measured non-invasively.

Effect of strain on resonant frequency:

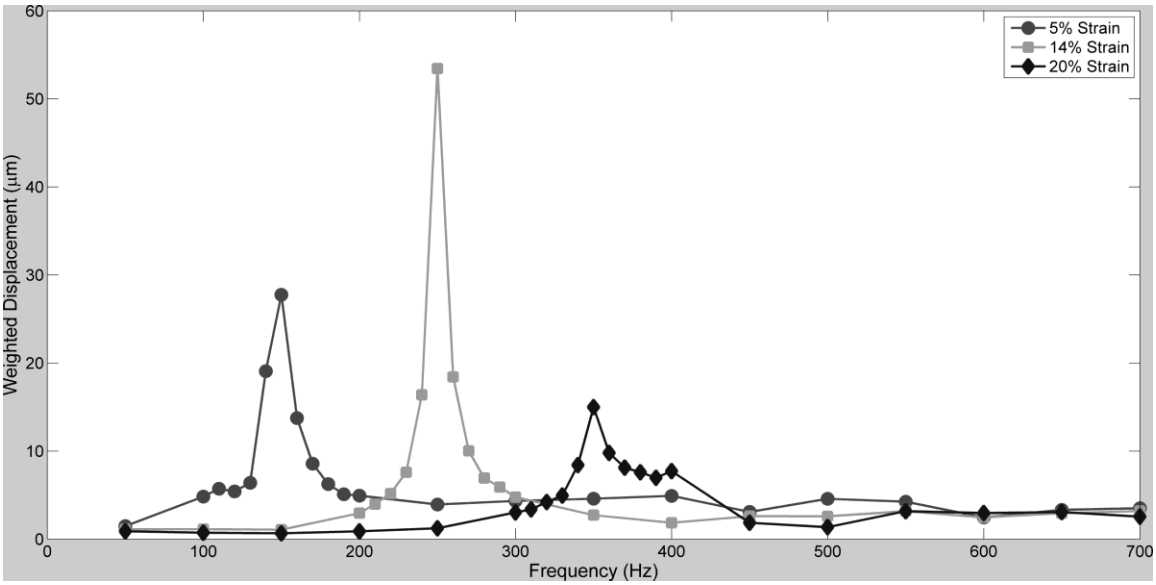

Figure 16. Plot of displacement versus frequency of vibration for decelluralized dermis at 5%, 14% and 20% strain. Note the maximum frequency increases with increasing strain.

The resonant frequency of the decellularized dermis sample increased with strain (**Figure 16**). The decellularized human dermis sample contains a single component i.e. collagen fibers. The modulus of collagen fibers in the skin increases from about 2.45 MPa (5% strain) to 13.36 MPa at a strain of 20%. The resonant frequency and calculated modulus are therefore dependent on the tissue strain and the composition. The fiber composition of collagen in the skin is usually random and the different collagen fibers align and disorient as the strain varies. The number of collagen fibers oriented in a given direction at a given strain can alter the sample vibrations induced by an external force, and can be the reason behind the difference in the weighted peak displacements of the dermis sample observed at different strains in **Figure 16**.

Multiphasic samples:

When pig dermis, consisting of epidermal and dermal layers, was tested using vibrational analysis and OCT, two natural frequencies were observed: one at 90 Hz and the other at

about 200 Hz as shown in **Figure 17** and **Table 3**. These peaks correspond to moduli of ~0.75 MPa and ~3.55 MPa, respectively at a strain of 5%. The peak at 200 Hz appears to be the collagen peak since it has a modulus of about 3.55 MPa as opposed to the one for collagen in the decellularized dermis with a modulus of 2.45 MPa. Whereas the peak at 90 Hz is probably a peak due to elastic tissue since it has a modulus of 0.75 very close to that reported for elastic tissue in monophasic sample experiments.

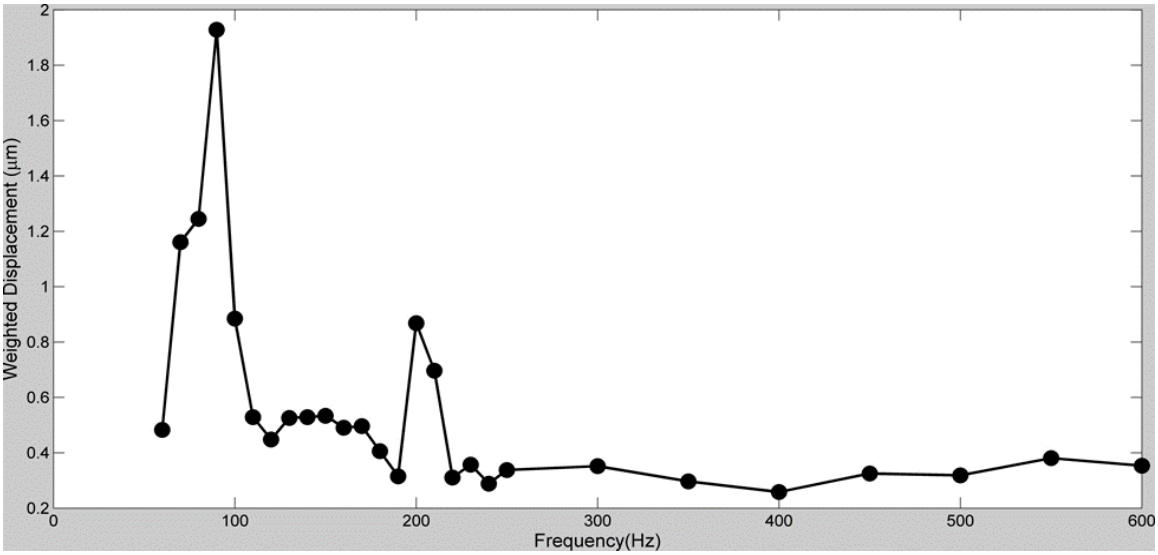

Figure 17. Measurement of the resonant frequency for pigskin sample using OCT and vibrational analysis. The two peaks shown correspond to the stretching of elastic fibers (90Hz) and collagen fibers (200 Hz).

Table 3. Resonant frequencies and moduli obtained from vibrational OCT for pigskin and bovine cartilage

Sample	Resonant Frequency (Hz)	Vibrational Testing Modulus (MPa)
Pig Skin	93.33 ± 5.77	0.77 ± 0.094
	203.33 ± 5.77	3.61 ± 0.2
Bovine Cartilage	246.67 ± 5.77	4.96 ± 0.23
	550 ± 10	24.65 ± 0.53
	663.33 ± 5.77	35.03 ± 0.61
Subchondral Bone	620 ± 10	31.92 ± 1.03

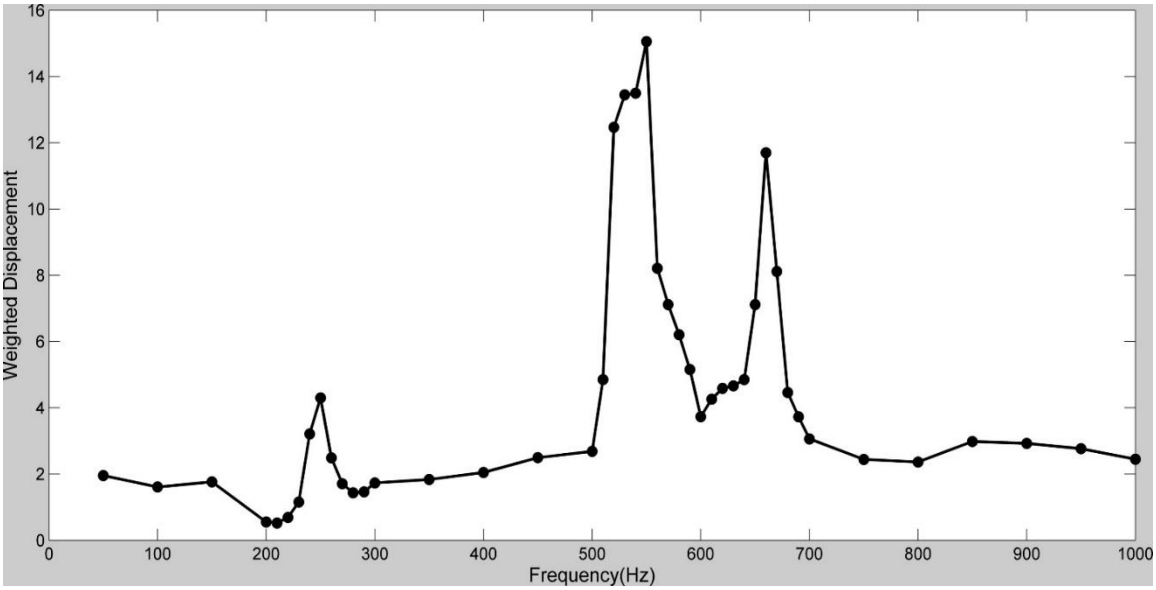

a)

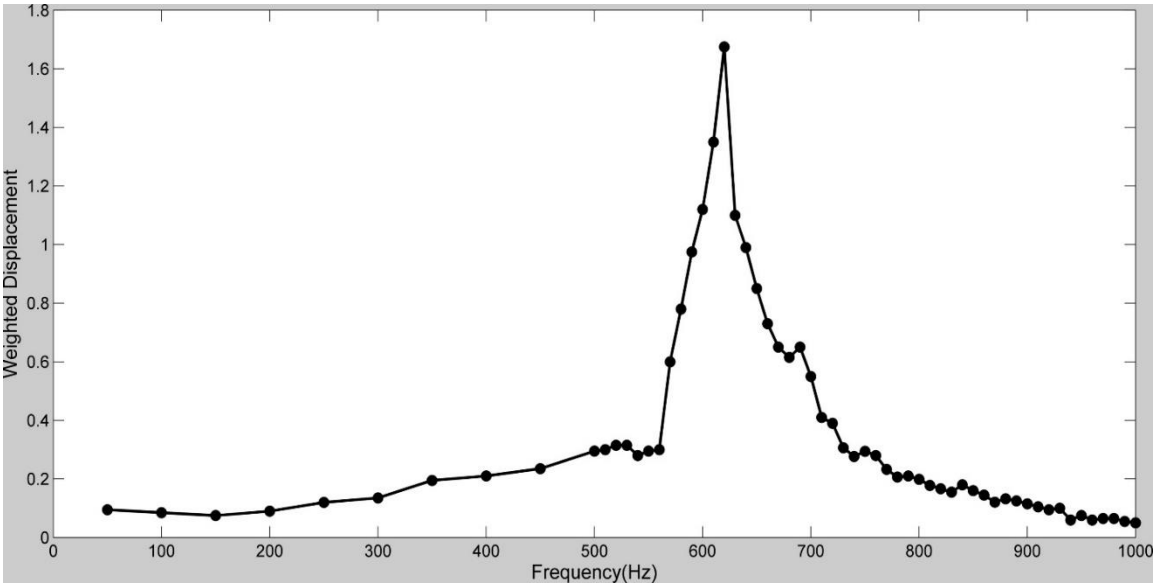

b)

Figure 18. a) Weighted displacement v. frequency for sample bovine femoral cartilage with a layer of subchondral bone. The resonant frequencies observed were 250Hz, 550Hz and 660Hz representing the moduli of 4.96MPa, 24.65MPa and 35.03MPa respectively. b) Weighted displacement v. frequency for sample bovine subchondral bone after the cartilage was removed with a scalpel. The resonant frequency was 620Hz and the modulus was 31.92MPa.

The bovine femoral cartilage demonstrated three resonant frequencies: one at 250 Hz one at 550 Hz and the final one at 660 Hz (**Figure 18a)**. The resonant frequency of subchondral bone was 620 Hz (**Figure 18b)** post-scraping off the cartilage from the subchondral bone using a scalpel.

The data obtained from bovine femoral cartilage (**Table 3**) suggests that the collagen peak at 250 Hz may reflect the collagen fibers in the superficial and intermediate zones. They have a modulus of 5.09 MPa, while the peak at about 620 Hz may reflect the behavior of the subchondral bone on which the cartilage rests since it has a modulus of >30 MPa. The peak at 550 may reflect the transition zone between calcified cartilage and the subchondral bone.

Preliminary *in vivo* results:

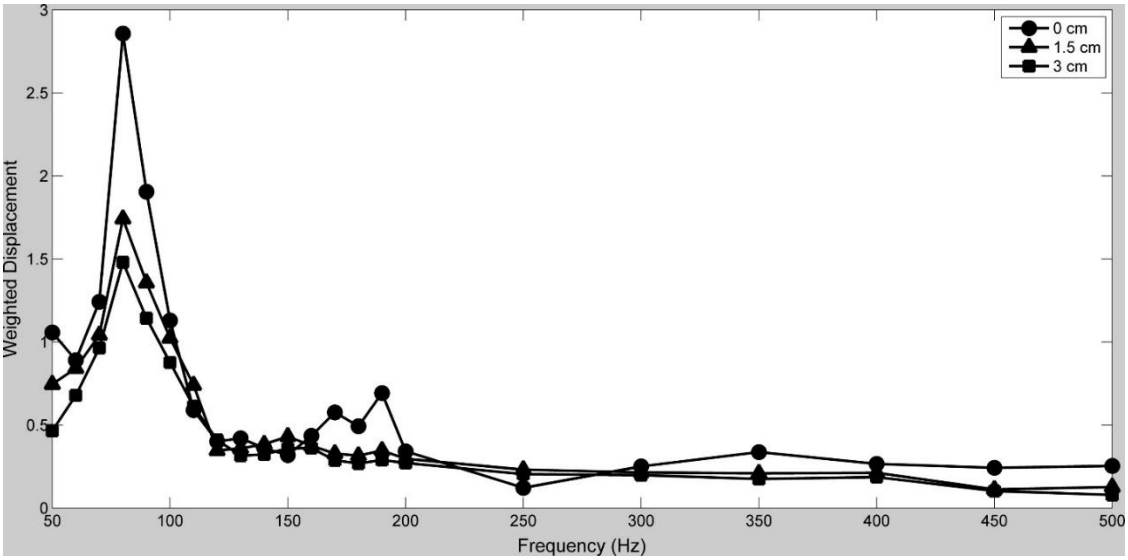

Figure 19. Plot of weighted displacement versus frequency for decellularized dermis at various separation distances between Digi-Key speaker and position of OCT light beam. The resonant frequency was found to be independent of the speaker placement. Only the amplitude of the displacement signal was found to be dependent on speaker placement using OCT and vibrational analysis.

Measurements of the resonant frequency made using the Intervox and Digi-Key speakers on the same piece of the decellularized dermis in vitro were found to be identical at strains of 2 to 15%. Using the Digi-Key speaker the resonant frequency of decellularized dermis was found to be independent of distance away from the speaker (**Figure 19**).

Measurement of the natural frequency of skin *in vivo* using the vibrational technique resulted in a single peak at 70 Hz as shown in **Figure 20a**. This peak corresponded to a modulus of 0.66 MPa. When vibrational analysis of scar tissue was carried out in an area within an inch of the measurements made on normal skin, the resonant frequency was increased to 220 Hz as shown in **Figure 20b**. This increase in resonant frequency corresponded to an increase in modulus to 4.2 MPa.

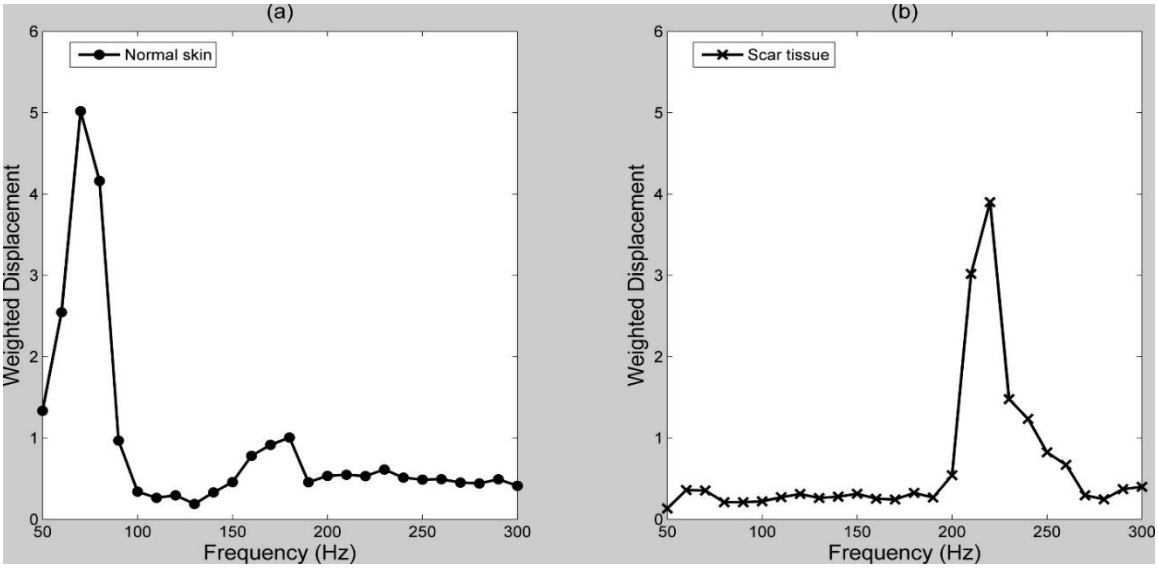

Figure 20. (a) Weighted displacement versus frequency for human skin made using OCT and vibrational analysis on human skin in vivo. The maximum weighted displacement and resonant frequency occur at 70Hz. (b) Weighted displacement v. frequency made using OCT and vibrational analysis on human scar tissue in vivo. The maximum weighted displacement and resonant frequency occur at 220 Hz.

The collagen peak in the normal skin measurements made *in vivo* is just a small hump in the curve. A possible reason may be that at low strains *in vivo,* the skin collagen fibers may be stretched minimally in tension, whereas the elastic fibers have been reported to bear the loads [15]. In contrast, in scar tissue, the collagen fibers bear all the tension, even at low strains since there is only a small elastic fiber peak in scar tissue. This is consistent with a previous observation that human hypertrophic scar tissue has the same stiffness as normal human skin even though it appears more rigid by palpitation [184]. The apparent increased stiffness of hypertrophic scar tissue is due to a reduced extensibility of this tissue and not an increased modulus [184] that occurs when elastic fibers are not replaced after a thermal injury.

The values obtained for the skin measurements in this study are higher than a similar OCE approach by Liang et al, 2010 that reported Young's modulus of ~100kPa for *in vivo* measurements on forearm [161]. However, the discrepancy in the values can be attributed to some of the key differences between the two studies. While the current method utilizes the resonant frequency of a material to compute the elastic modulus, Liang et. al use the surface velocity, driving frequency and the Poisson's ratio to compute the elastic modulus [161]. The current study measured the modulus on the dorsal side of the finger whereas Liang et al. performed their measurements on forearm and palm that may have different elasticity as compared to the test site in the current study. However, it has been seen that different testing methods result in different values of moduli for the same anatomical location; e.g. *in vivo* measurements on forearm have been reported to be around 0.1MPa by OCE and suction methods, whereas the values obtained using uniaxial and torsional tests have reported values of 1-3MPa [19,91,185,186]. Thus, *in vivo* conditions need to be assessed properly before choosing a testing method and comparison with a gold standard technique should be preferred to calibrate and assess the efficacy of a new

biomechanical testing method.

Summary

The results presented in this chapter suggest that a combination of OCT and vibrational technique can be used for non-destructive mechanical testing of tissues and materials. The moduli of soft tissues and polymeric materials obtained from this method are similar to those found using uniaxial tensile stress-strain measurements. The advantage of this method is that the modulus can obtained from vibrational methods without having to approximate the tangent to the stress-strain curve, which is difficult for non-linear materials that have a rapidly changing slope.

A calibration curve for the moduli computed using the vibrational OCT technique and uniaxial tensile test showed a slope of almost 1, thereby validating the use of this technique for nondestructive biomechanical testing. This technique was also useful in determining the effects of strain on the elasticity of dermis, and to study the effects of chemical treatment on allografts.

The vibrational OCT method proposed in this chapter was also successful in performing mechanical spectroscopy of multiphasic samples like pigskin and bovine cartilage by identifying distinct resonant frequencies of various tissue components. Preliminary *in vivo* test were able to differentiate between normal skin and scar tissue. With more tests and a better calibration for the *in vivo* tissue conditions, this technique may be useful to evaluate the extent of wound healing in skin diabetic ulcers and other chronic skin conditions, scar tissue formation in response to implants, and other therapeutic treatments that alter ECM properties.

CHAPTER 3: MEASUREMENT OF VISCOELASTIC MODULUS USING VIBRATIONAL OCT SETUP

Note: Portions of this chapter have been published in the following citations and represent the original work of the candidate:

1. Shah, R. G., & Silver, F. H. (2017). Viscoelastic Behavior of Tissues and Implant Materials: Estimation of the Elastic Modulus and Viscous Contribution Using Optical Coherence Tomography and Vibrational Analysis. Journal of Biomedical Technology and Research, 3, 105-109.
2. Silver, F.H., Silver, L.L., Shah, R.G., 2017. Viscoelastic behavior of allografts and scaffolds composed of extracellular matrix. Adv in Tissue Eng Regen Med 2 (1): 00019. DOI:10.15406/atroa.2017.02.00019.

Specific Aim 2

Compute viscoelastic properties of decellularized dermis using vibrational OCT system.

Hypothesis and Rationale

Most biological materials are viscoelastic in nature i.e. the phase between the stress and the strain cycles is >0º and <90º (**Figure 21**). The modulus of a viscoelastic material can

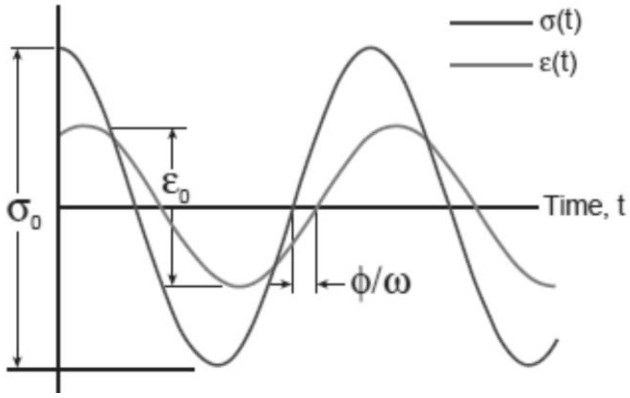

Figure 21. Cyclic stress (σ_0) v. strain (ε_0) cycle of viscoelastic material. Φ is the phase difference and ω is the loading frequency of stress.

be broken into two components: Storage Modulus and Loss Modulus. The storage modulus relates to the elastic behavior of the material and the loss modulus relates to the viscous component of the material. Apart from other parameters, temperature and frequency affect the viscoelastic behavior the most.

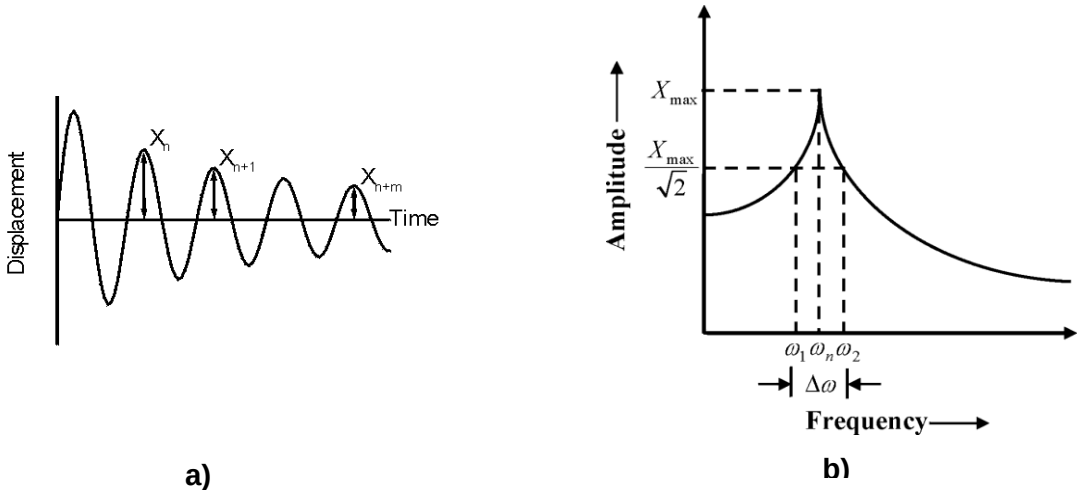

Figure 22. a) Transient response of a classically damped SDOF underdamped system. b) Compliance transfer function of an underdamped system. ω_n is the driving frequency, $\Delta\omega$ is the bandwidth of the frequency range having power 3db below the peak X_{max} that has an amplitude of $X_{max}/\sqrt{2}$. (Reproduced from Singh et al., 2012)

Many elastography techniques model tissues by ignoring the viscosity portion of their behavior [111,115]. It has been shown that a material exhibits elastic behavior when vibrated at its natural frequency [179,187]. The main hypothesis of this aim is that the material responds as almost purely elastic at its resonant frequency, whereas its viscoelastic nature comes into play at other frequencies in terms of energy dissipation of impact loads. Thus, dermis will show the response of a single degree of freedom (SDOF) underdamped system (**Figure 22a)** and will demonstrate elastic and viscoelastic properties when pulse-vibrated at resonant and non-resonant frequencies, respectively. The percent of loss modulus contributed by the viscous component of the tissue's behavior

over a range of stimulation frequencies will be computed by using the half-power bandwidth method [188] (**Figure 22b**) and the results should be comparable to that in the literature.

Experimental Methods

Decellularized human dermis, silicone and pigskin samples were used for this experiment. The sample preparation and dimensions were same as that used in the experiments for Aim 1. In order to compute both, the viscous and elastic components of the tissue, it is necessary to compute the phase lag between the stress and the strain cycles. Another way to compute the viscoelastic nature is to observe the decay response of the sample when vibrated with an impulse or a burst of few sinusoidal cycles as a viscoelastic material behaves like an underdamped system whose storage and loss moduli can be computed using the half-power bandwidth method. In this study, the benchtop setup was modified such that the function generator drove the Intervox speaker (that was used for Aim 1 experiments) with bursts of three cycles of sinusoidal waves. It has been shown that skin exhibits viscous response up to 600Hz [55]. Thus, two sets of frequency ranges were chosen for this Aim: 1) 10Hz to 100 Hz in steps of 10 Hz for human dermis at 5% strain, and 2) 50 Hz to 600 Hz in steps of 50 Hz, for human dermis, silicone and pigskin. In order to observe the loss modulus at the resonant frequency, resonant frequencies of the samples were computed as per the procedure specified in the experiments of Aim 1. For this second set of experiments, the human dermis and silicone samples were tested at strains of 5%, 10% and 15%, whereas the pigskin samples were tested at 3% and 7% strains as the slippage make it difficult to strain the pigskin at higher strains.

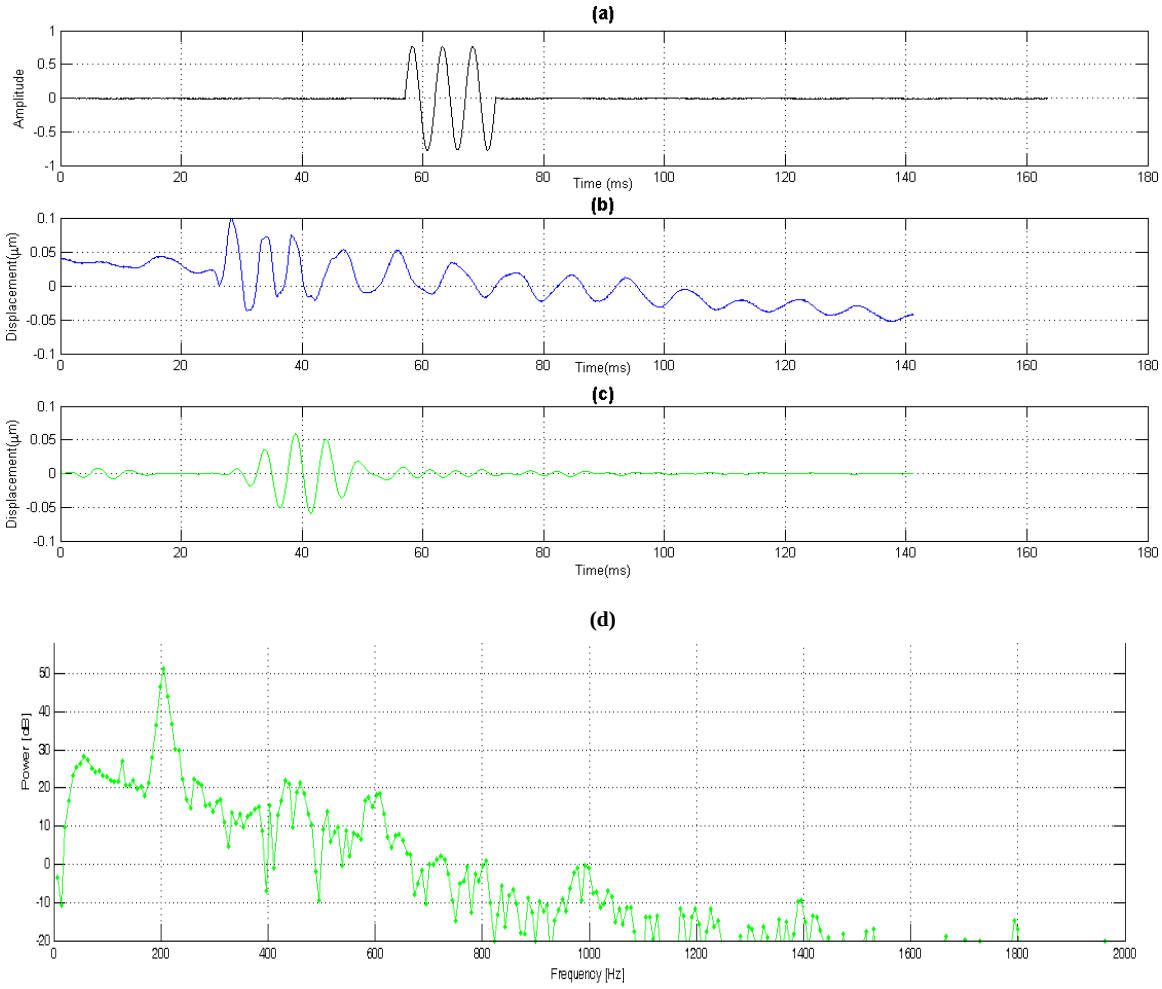

Figure 23. Illustration of the input and output waves of the viscoelasticity experiment. (a) Amplitude v. time plot of the 3-cycle sinusoidal input wave; (b) Raw output of sample displacement v. time showing the decay response of the sample; (c) Band-pass filtered output of displacement v. time. (d) Frequency response of the sample displacement. Note: the lag in the input and output waves is due to a minor time difference in capturing the input and output waves.

When vibrated with pulsed input waves (**Figure 23a**) the samples exhibit response similar to that of an underdamped system i.e. a sinusoidal response that decays with time (**Figure 23b**) [189]. The displacement data was bandpass filtered as in Aim1 to remove the electrical noise and other frequencies (**Figure 23c**). The half-power bandwidth method

that is generally used to quantitatively measure the damping η or loss factor [190] was used to determine the loss modulus percent of the samples at different strains. The frequency response of the material is plotted in terms of frequency v. power (**Figure 23d**). The loss factor, η, was computed as the ratio of the driving frequency, ω_0, and the bandwidth of the frequency range for which the power reduces to half of the power at the peak resonant point, Δω. In decibel scale, this occurs at 3db below the peak value. The loss factor was computed at each driving frequency for each sample at different strains.

Results and Discussion

Below 100 Hz:

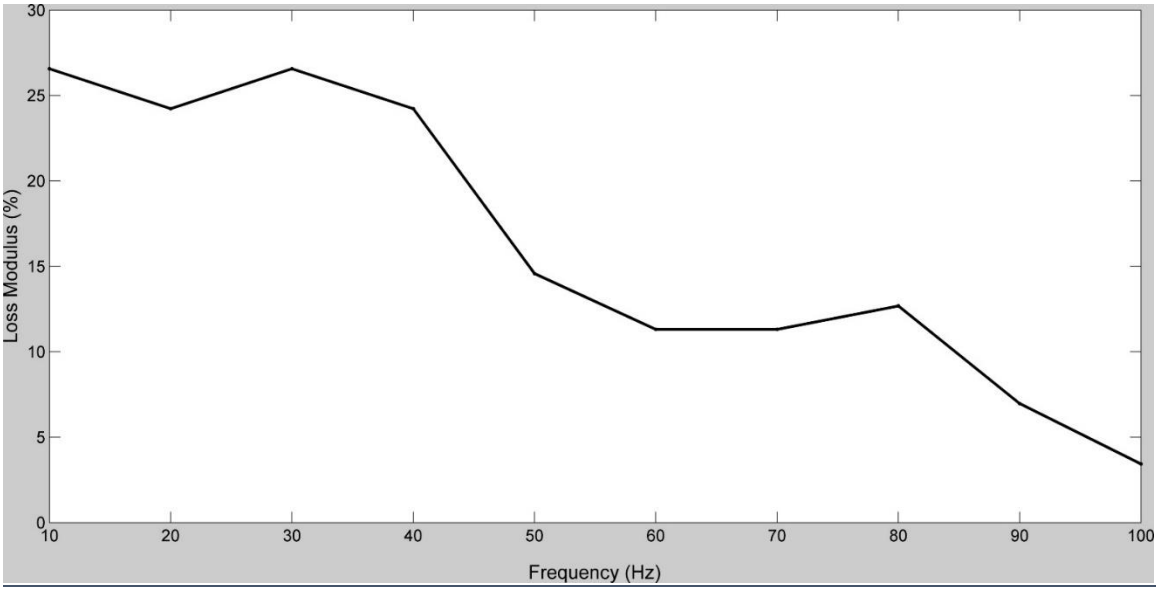

Figure 24. Plot of frequency v. loss modulus percent for decellularized wet dermis at 5% strain. The dermis is highly viscous below 100 Hz but shows only 3.4% loss modulus at its resonant frequency, 100 Hz.

The wet decellularized dermis showed loss modulus percent of up to 27% below 100Hz (**Figure 24**). The loss modulus values gradually decreased as the driving frequency approached 100 Hz, which also happened to be the natural frequency of the sample. The

results of this experiment are similar to that shown by [191], who studied the effect of frequency on loss modulus for rabbit skin (**Figure 25**). Their results also showed high loss modulus below 100 Hz. This is in concert with other studies that have shown that skin is more viscous at low frequencies [190,191].

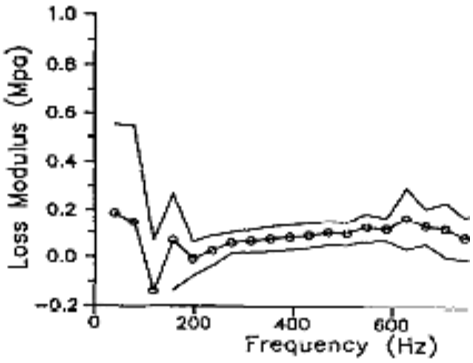

Figure 25. Frequency v. Loss Modulus for rabbit skin (Reproduced from Pereira et al.; 1991)

Above 100Hz:

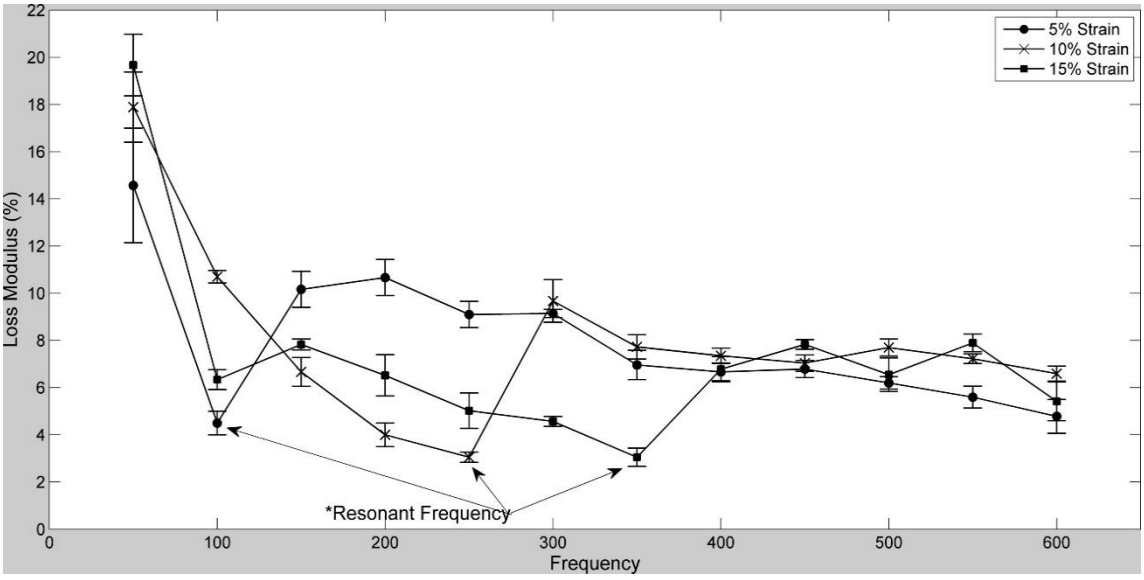

Figure 26. Plot of loss modulus as a percent of total modulus based on the half-power bandwidth method for decellularized dermis at strains of 5%, 10% and 15%. Note the resonant frequencies are 100Hz (5% strain), 250 Hz (10% strain) and 350 (15% strain).

The plots for loss modulus as a percentage of the total modulus for decellularized dermis, silicone rubber and pigskin are shown in **Figure 26, Figure 27** and **Figure 28** respectively. The loss modulus exhibits minimum value at the resonant frequency. At the resonant frequency, the loss modulus is approximately 3% to 4% of the modulus value reported.

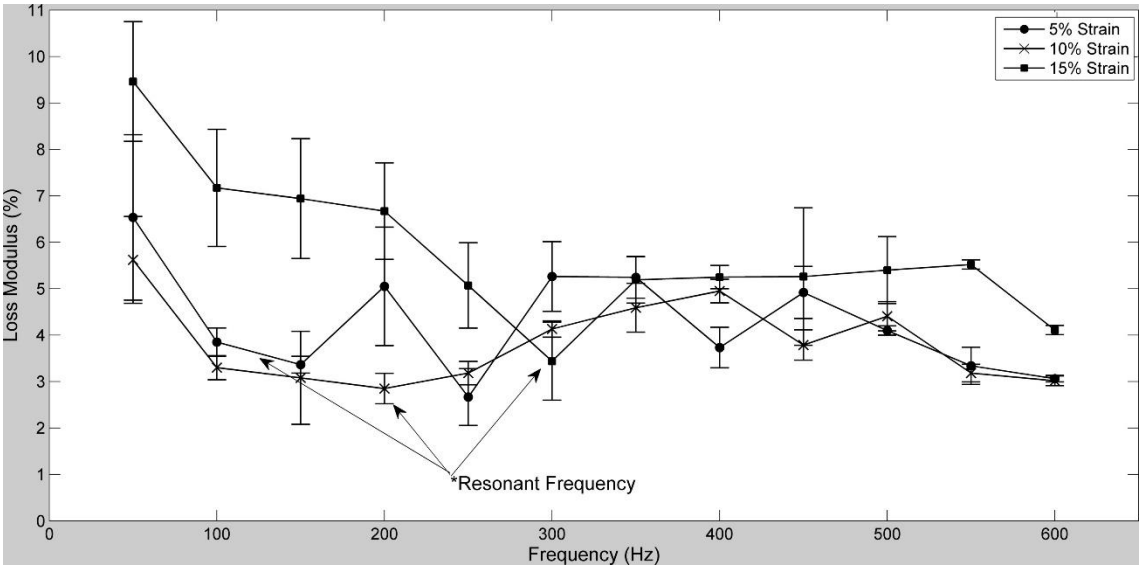

Figure 27. Plot of loss modulus as a percent of total modulus based on the half-power bandwidth method for silicone rubber at strains of 5%, 10% and 15%. Note the resonant frequencies were 120 Hz (5% strain), 200 Hz (10% strain) and 300 Hz (15%). The viscoelastic testing was not performed at 120Hz. The resonant frequency at 5% strain was measured in a prior report and was not a multiple of 50Hz [28].

The results suggest that the modulus calculated at the measured resonant frequency is a good estimate of the elastic modulus of the material. The value of the viscous component of the modulus of a material at the resonant frequency can be as low as 3% to 4%. At lower and higher frequencies than the resonance frequency, the loss component of the modulus increases. Modulus measurements made at the resonant frequency of skin appear to be primarily a result of elastic deformation while those made at lower frequencies appear to contain a significantly larger viscous contribution. At frequencies

above the resonant frequency, the viscous contribution appears to rise above that observed at the resonant frequency but remains relatively low.

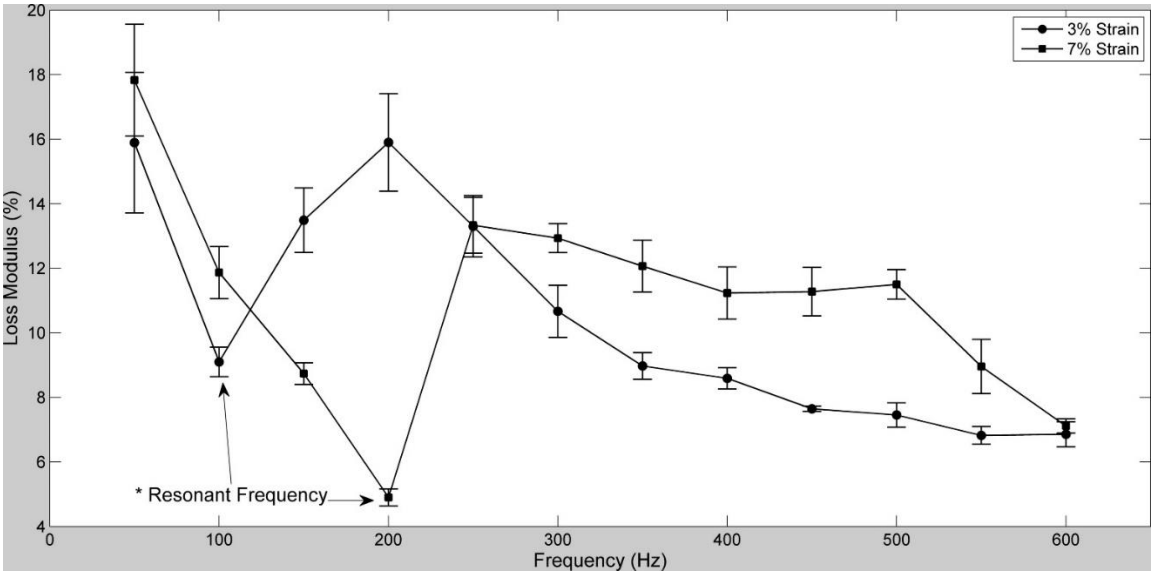

Figure 28. Plot of loss modulus as a percent of total modulus based on the half-power bandwidth method for pigskin at strains of 3% and 7%. The resonant frequency was 100 Hz (3% strain) and 200 Hz (7% strain).

Summary

Viscoelasticity of collagenous tissues is important in resisting impact loads especially in the musculoskeleton; however, it complicates the understanding of ECM behavior since most real-time measurement techniques made on these tissues neglect the viscous contributions. However, most biological tissues (e.g. skin) are non-linear and viscoelastic and have an upward curvature to the stress-strain curve. This fact makes determination of the stiffness using the stress-strain curves difficult since the tangent to the stress-strain curve is constantly changing.

This section reported the experiments of using bursts of sinusoidal cycles in conjunction with OCT to assess the viscoelastic mechanical properties of ECM and silicone rubber at

frequencies above and below the resonant frequency. The results reported suggest that measurement of the modulus at the resonant frequency of a viscoelastic material provides a good estimate of the elastic modulus while measurements below and above the resonant frequency contain a larger viscous contribution to the viscoelastic behavior. It was also seen that the viscous contribution is greater at lower frequencies (<100Hz), an observation that matched results from other studies in the literature.

During mechanical loading, a tensional increase in the D period of a collagen molecule is observed with increasing strain and is associated with: 1) elongation at the triple-helical level of structure in the flexible regions; and 2) increase in the gaps between the distance of two triple helices in the microfibril. Additionally, tension leads to some molecular slippage that may cause viscous energy loss [192]. Molecular stretching is known to occur at lower stresses; whereas the increases in the gap spacing and molecular sliding occur at higher stresses [193]. Molecular stretching and slippage are reversible over time. It is believed that molecular stretching begins in the regions devoid of proline and hydroxyproline, the charged regions of the sub-bands in the D period. At higher strains, the stress-strain behavior in tension becomes reversible and collagenous materials fail by defibrillation [25].

The healing response in bones and tendons that is attributed to high frequency loading mechanism of the extracorporeal shock wave therapy probably involves tensile stretching of the collagen fibers in tissue that upregulates mechanotransduction through an integrin mediated pathway [183,194]. Along these lines the low energy dissipation of collagen in skin may prevent premature mechanical failure at frequencies less than ~100 Hz, while at frequencies above 100 Hz extracorporeal shock wave may promote mechanotransduction at the collagen fiber and cellular levels to promote healing.

As the frequency of mechanical deformation increases, network strands in the collagen molecule fail progressively to adjust themselves in the time provided by the frequency of the oscillations. At intermediate frequencies, the molecules form unstable cross-links to effectively transmit the mechanical forces. At lower frequencies, the entire molecule moves at a slow pace and provides the molecules with an opportunity for energy dissipation; thereby increasing the viscous component of the modulus at frequencies <100 Hz. At resonant frequencies, the collagen molecules move almost in the same phase as the imposed oscillations in order to create the maximum displacement. This lack of phase difference is evident by the almost purely elastic response of the test materials at resonant frequencies.

It can be concluded that at low strains the high viscous contribution to the modulus of the skin may provide a mechanism for energy dissipation of impact loads while the low viscous contribution to the modulus of skin at the resonant frequency may promote mechanotransduction.

CHAPTER 4: MEASURES OF BIOMECHANICAL PROPERTIES OF CHORIONIC PLATES FROM EARLY, NORMAL AND PATHOLOGICAL PREGNANCIES

Specific Aim 3

To characterize/differentiate chorionic plate tissues from normal, pathological and early term pregnancies through the use of vibrational OCT setup.

Hypothesis and Rationale

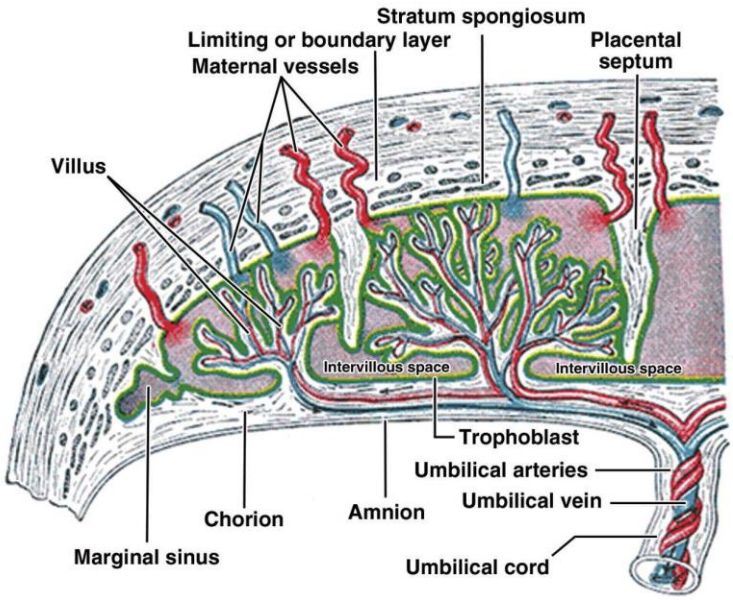

Figure 29. Structure of placenta. Reproduced from Gary, 1918.

The chorionic plate carries the large vessels that are the first branches off the umbilical arteries and the umbilical vein once the cord inserts on the chorionic plate. These large vessels are fetal blood vessels and important conduits of oxygen, nutrient, and waste from and to the fetus. The chorionic plate and the surface vessels form the fetal side of the placental disc (**Figure 29**, [3]). The plate is comprised of amnion (most internal to the fetus) and chorion, and villi arise from its outer surface [195]. Its proper growth and development is crucial for proper functioning of a normal placenta. The intervillus space

and size differ between a normal and a diseased placenta (**Figure 30**, [196]). Diabetic placentas have large villi with a dense distribution [197], whereas pre-eclamptic placentas typically have sparse and small villi [198] as compared to a normal placenta. Villus immaturity and chronic fetal hypoxia are prevalent in diabetic placentas that result in a lower fetal/placental weight ratio and higher frequency of fetal complications as compared to normal placentas [199,200]. One of the objectives of this aim is to test if this variation of phenotypes is translated to the biomechanical properties of the respective chorionic plates.

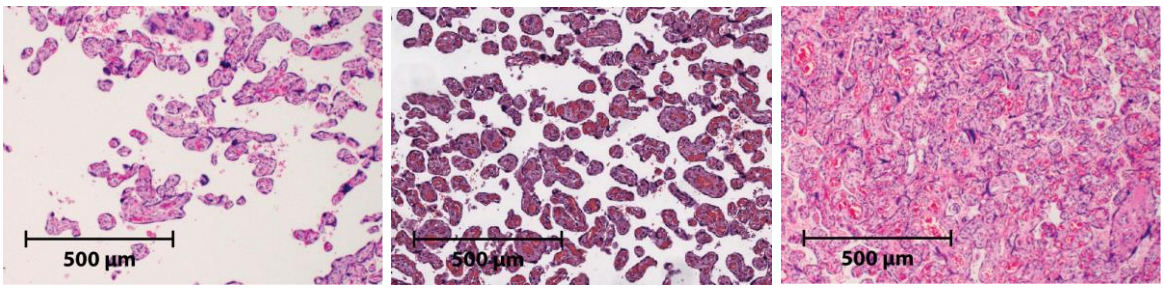

Figure 30. Typical cross-sections of a) pre-eclamptic b) normal and c) diabetic placentas. Pre-eclamptic placentas have sparse villus distribution and diabetic placentas have a dense villus distribution. (Adapted from Serov et al. 2015)

ECM provides angiogenesis with its crucial framework through structural support and molecular interactions. Mechanical traction forces applied by neovessels and the resulting ECM deformation are key regulators of growth, neovascularization and angiogenesis [201–203]. Thus, biomechanical properties like viscoelasticity of tissues should greatly influence angiogenesis. The chorionic plate of the human placenta is known to have a distribution of a range of collagen fibers, the composition and orientation of which change over the gestation [174,204].

The primary hypothesis of this aim is that the vibrational testing moduli of chorionic plates from normal pregnancy will vary across gestation, and in health and disease. If correct,

our future studies will explore if these variations correlate with altered vasculature, villus distribution, and tissue composition. The physiological changes in the villi and the intervillous space would affect the biomechanical properties of the chorionic plate or vice versa. However, in order to study the effect of gestational age and pathology on the chorionic plate biomechanics, the samples used for this study consisted of just the 'chorion' layer as seen in **Figure 29**, a connective tissue membrane containing fetal vessels, internal to amnion, external to chorionic villi. The chorionic villi were scraped and the amnion layer was pulled to separate the chorionic plate sample for each placenta.

Experimental Methods

Table 4. Description of pathological placentas

Placenta ID	Pathology
6	Category 2 Fetal heart rate tracing
7	Chronic Villitis and acute intraamniotic infection
8	Diabetes Mellitus
9	Acute intraamniotic infection
10	Small growth-restricted placenta (Pre-eclampsia)

The chorionic plate sections from 5 normal at term, 5 pathological (see **Table 4** for description) and 2 pre-eclamptic placentas were obtained immediately post-delivery. They were cut from the insertion point extending radially towards the placental edge and stored in phosphate buffered saline (PBS) azide to avoid bacterial growth. Chorionic plate sections from three 15-week placentas were similarly obtained from an early termination clinic. All tissues were collected under IRB approval. The sections of chorionic plates were thoroughly washed in PBS to remove blood, scraped with a scalpel to remove the underlying villous structures and stored back in PBS azide. All the samples were tested within 48-72 hours of collection.

The chorionic sections were trimmed with regular scissors to obtain rectangular pieces of approximately 1.5cm x 7cm for testing with the vibrational OCT setup. The samples were clamped and stretched to reach a 3% strain. Three runs of vibrational testing (as described in Chapter 2) was performed at the center and at 4 edges of each sample for consistency (**Figure 31**). The dimensions of each sample were measured using digital calipers and the weight was measured using a digital scale. For a couple of normal pregnancy samples, the chorionic plates had portions of surface vessels. Vibrational OCT readings were taken on a point on these surface vessels for the relevant samples.

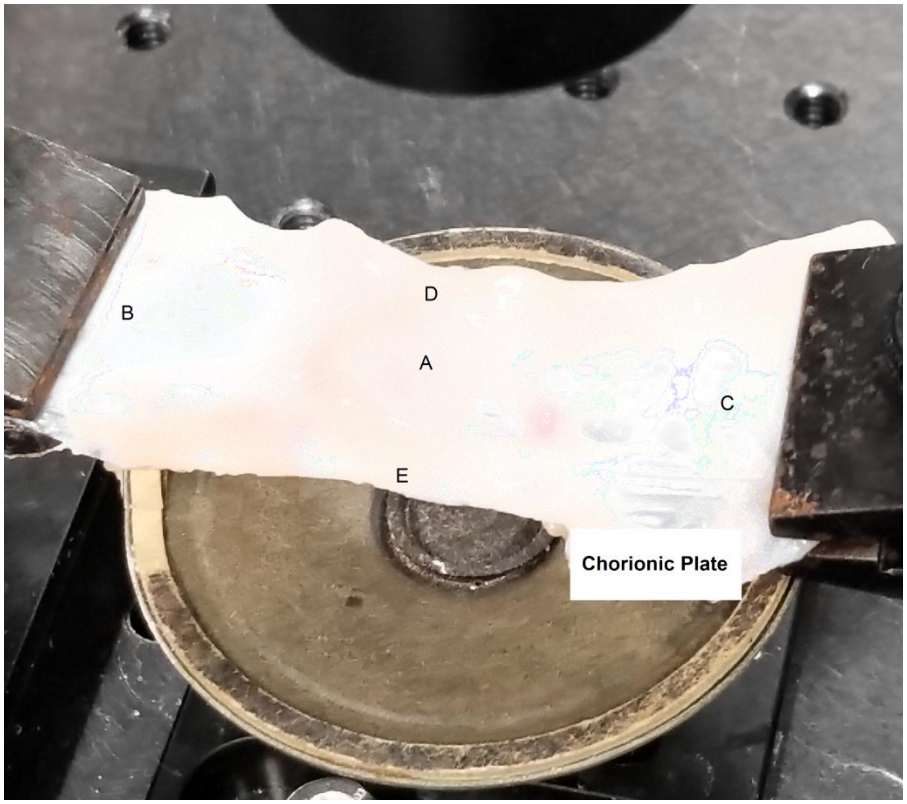

Figure 31. Typical chorionic plate sample used for vibrational OCT testing. Points A-E show the regions where testing was performed.

Statistical Analysis: The vibrational OCT moduli were divided into three groups: early-term, normal and pathological (including the pre-eclamptic samples). Since the output in this study was only one independent variable i.e. modulus, the one-way statistical tests were

used. One-way ANOVA and Kruskal-Wallis one-way analysis of variance tests were performed using SPSS 23 (IBM, Chicago, IL) on these moduli to test whether there was any statistically significant difference in the moduli of different groups. The Kruskal-Wallis test is a non-parametric test to determine whether two or more groups of an independent variable are statistically different [205]. The one-way ANOVA is a parametric test used to compare the means of two or more groups for statistical differences [206].

Results and Discussion

Table 5. Vibrational OCT testing moduli for chorionic plates of normal, pathological, pre-eclamptic and early term placentas

Placenta ID	Type	Modulus (MPa)
1	Normal	0.65 ± 0.082
2	Normal	0.79 ± 0.071
3	Normal	0.72 ± 0.059
4	Normal	0.62 ± 0.047
5	Normal	0.69 ± 0.036
6	Pathologic	1.1 ± 0.094
7	Pathologic	1.81 ± 0.112
8	Pathologic	1.01 ± 0.083
9	Pathologic	1.33 ± 0.077
10	Pathologic	0.92 ± 0.113
11	Pre-eclampsia	1.17 ± 0.085
12	Pre-eclampsia	1.18 ± 0.043
13	15-week early term	0.33 ± 0.026
14	15-week early term	0.27 ± 0.101
15	15-week early term	0.38 ± 0.091

The vibrational testing for the normal pregnancy group differed from those of the pre-eclamptic group and early term group (**Table 5**). The early-term group showed a mean modulus of 0.33 MPa, slightly less than half of the average modulus of the normal/ control group (0.69 MPa). The average modulus of the samples from the pre-eclamptic group was 1.18 MPa, almost equal to 1.24 MPa, the average modulus of the pathological pregnancies group.

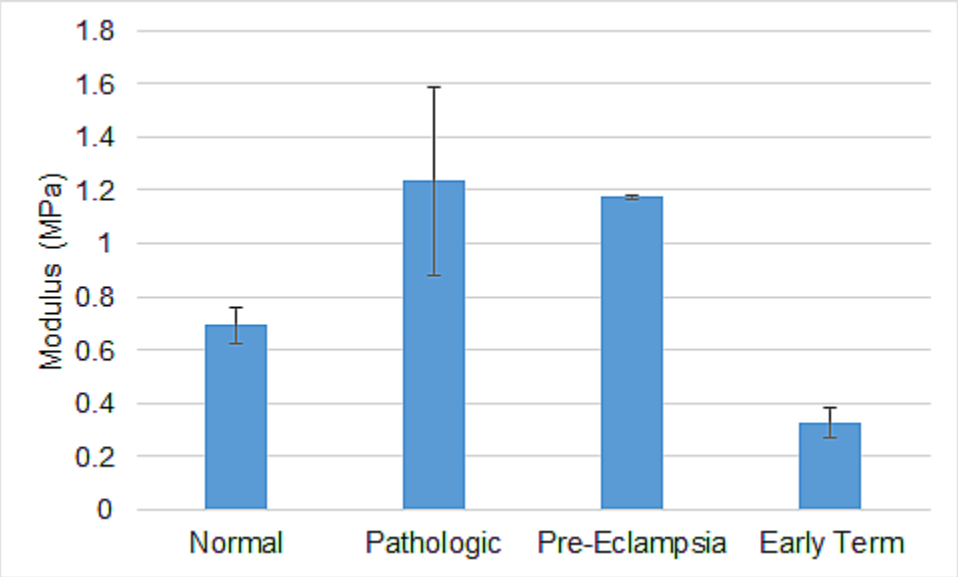

Figure 32. Moduli for normal, pathological, pre-eclamptic and early-term pregnancies obtained using the vibrational OCT setup. The errorbars represent the standard deviations of the mean moduli obtained using vibrational OCT for samples of each cohort.

The statistical analysis were performed by considering the pre-eclamptic cases as a subset of the pathological cases. The one-way ANOVA test showed that the three groups - normal, pathological and early-term, were significantly different with a $p<0.001$; whereas the Kruskal-Wallis test showed that the three groups were significantly different with a $p=0.002$.

The measurements taken on the vessel surfaces showed a higher resonant frequency as compared to the corresponding chorionic plates. The complex geometry of the vessels

made it difficult to measure their proper dimensions in order to compute a modulus as per Equation 3. The presence of the blood vessels has been assumed to result in a higher elastic modulus for the chorionic plate region as compared to the maternal surface [207]. The higher resonant frequencies for the surface vessels observed during the OCT vibrational testing is somewhat in line with this assumption.

Acoustic radiation force impulse elastography measurements that have shown that pre-eclamptic placentas are stiffer than normal placentas [208,209]. Pre-eclampsia has been associated with a thicker basement membrane of chorionic villi [198] and a stiffer umbilical artery [210]. The current study's observation of a significantly higher average modulus of pre-eclamptic placentas as compared to the control group (**Figure 32**) matches the other clinical observations listed above. The stiffer matrix should affect the blood flow that is vital to the proper growth of the developing fetus.

The histological sections of early-term placentas appear sparse under the microscope. The connective tissue component in the early stage is mostly fibrous and loosely arranged. The fetal vessels are generated via vasculogenesis and branching angiogenesis during the first and the second trimesters [211]. A more compliant matrix may help the fetal vessels to branch and grow, an important characteristic in the early developmental stage.

The chronic villitis is generally known to cause the inflammation of the villi [212–214], whereas the acute intraamniotic infection or chorioamnionitis is the bacterial infection that leads to inflammation of the fetal membrane [215,216]. Thus, the significantly higher moduli of the two placentas with acute intraamniotic infection seem clinically relevant. Especially, the placenta with chronic villitis and acute intraamniotic infection had the highest modulus among all the placentas tested.

Although the moduli of the pathological placentas were significantly higher than the normal group, they showed some unexpected results. For instance, the chorionic plate from the diabetic pregnancy showed a modulus lower than some of the other pathological pregnancies. Diabetic placentas are known to have larger and dense villi, and a smaller number of surface vessel branches. Thus, the assumption was that the chorionic plate of the diabetic placenta would be significantly stiffer, and thereby support the hypothesis that stiffer matrix results in poor angiogenesis. Small growth-restricted placentas have been shown to have a significantly higher stiffness as compared to the normal placentas [217]. Our results for the small growth-restricted placenta are significantly higher than the normal placentas; however, they are lower than the other pathological placentas (**Table 5**). It was expected that the small growth-restricted placenta would show the highest stiffness as that would corroborate the clinical reason for an inefficient placental function.

Summary

This study was clearly able to differentiate the chorionic plates of the normal pregnancies from early-term and pathological cases. Chorionic plates from pathological placentas (e.g. pre-eclamptic, diabetic, and growth-restricted) were stiffer as compared to chorionic plates from placentas of comparable gestational ages. Although a larger sample size will help to properly categorize the different pathologies based on their biomechanical properties, this is a promising biomechanical test for the pharmaceutical and medical industries that use collagen extracted from placentas for biomedical purposes [218–221]. Also, further studies are required to test the correlation of these different moduli to chorionic surface vasculature, which if present, will be the base of future experiments to study which factor plays the cause and which one is the effect.

Collagen type IV, the major component of chorionic plates and all basement membranes, defines integrity, stability and functionality that is required during the various

developmental stages of the fetus [222]. As expected, the moduli obtained for the chorionic plates in this study were lower than those obtained for the dermis whose major components are type I and type III collagen.

CHAPTER 5: SUMMARY AND FUTURE WORK

The results presented in this dissertation suggest that vibrational analysis done in conjunction with OCT is a promising tool to non-destructively evaluate mechanical properties of ECM in animals and humans as well to provide morphomechanical analyses of tissues and implants. This study successfully employed vibrational technique in association with OCT to obtain the resonant frequencies of soft tissues and compute their elastic moduli.

The calibration curve plotted for the results obtained from the vibrational OCT technique and the uniaxial tensile tests, a gold standard technique, on the same samples was a major plus for the proposed technique. Other elastography techniques need to conduct such experiments in order to confirm the results obtained from their methods that are based on multiple assumptions that may generate errors in their output parameters leading to a discrepancy in the values of the mechanical properties of a tissue measured using different techniques.

This methodology allows for correction for viscoelastic effects and provides valuable information about the behavior of tissues, both normal and pathological, and that of implants used to replace tissue and organ function. The results of studies on chemically treated decellularized dermis suggest that vibrational analysis is a useful technique to look at changes in the properties of allografts and implants post-treatment. An apparatus based on this methodology that can provide real-time measures of material's mechanical properties can aid surgeons in an operating room to analyze the viscoelastic properties of allografts and implants that they will be putting in a patient's body. The detection of the Langer's lines in order to align them in the host tissue and the allograft would be of vital importance to avoid implant failures at the interface that lead to multiple surgical corrections adding up to billions of dollars in cost every year. Other potential applications

of this technique include studying the effects of aging, cosmetic surgeries and other treatments on skin. It can also be used to test the efficacy of beauty products in terms of hydrating and/or softening the skin.

The viscoelastic studies not only computed the loss modulus but also provided further evidence that ECM is almost purely elastic when vibrated at the resonant frequency. Future technological advancements of this technique should work to compute the viscoelastic properties of soft tissues in real-time like the ability of impulse-excitation based commercial systems that can evaluate the viscoelastic properties of solid elastic materials in real-time.

The ability to extend *in vitro* measurements to *in vivo* assessments on skin and scar suggest that this method can be a useful tool to evaluate processes that alter skin properties in animals and humans as well to study the onset and pathogenesis of skin diseases such as cancer. Further studies are needed to properly calibrate this technique for *in vivo* applications as the tissue geometry is non-linear and tissue environment plays a major role in its functionality. This technique can be potentially be used to evaluate the extent of wound healing in skin ulcers and other chronic skin conditions. Such real-time non-invasive approaches can prevent the need of skin biopsies and save patient time, money and discomfort.

The results from the placental experiments demonstrated significant differences in biomechanical properties of the chorionic plates of the early-term, normal and pathological pregnancies. Even though OCT does not have a penetration depth of ultrasound or MRI that can be used for imaging during pregnancy, this technique can be useful in establishing a ground truth about the mechanical properties of normal and pathological placentas. Future studies with a higher sample size will allow to further establish the differences in the biomechanical properties of normal and pathological placentas. Those can then be

correlated with morphological and branching characteristics of placental vasculature to understand any potential relationship between angiogenesis in placenta and its biomechanical properties. Such studies can also be used to evaluate whether poor angiogenesis is caused by stiffer placentas or is the cause-effect cycle other way around. Once these research studies establish the clinical parameters to be observed, UE or MRE can be used to monitor pregnancies and aid in early diagnosis of potential problems based on their mechanical properties.

This thesis makes a strong case for using the vibrational technique with OCT in order to evaluate biomechanical properties of tissues and implants nondestructively. However, the studies reported in this dissertation employed OCT to only measure the displacement of the test samples induced by a vibrating speaker. Future studies can utilize the imaging functionality of OCT in order to obtain high resolution two-dimensional images or three-dimensional volumes of the tissue and overlay stiffness information on them to obtain elastograms of great clinical importance.

Bibliography

1. Millington PF, Wilkinson R. Skin. Cambridge University Press; 1983.

2. McGrath JA, Eady R a. J, Pope FM. Anatomy and Organization of Human Skin. Rook's Textbook of Dermatology. Blackwell Publishing, Inc.; 2004 p. 45–128.

3. Gray H. Anatomy of the human body. Lea & Febiger; 1918.

4. Agache P. Physiologie de la peau et explorations fonctionnelles cutanées [Internet]. Paris: Editions M´edicales Internationales; 2000.

5. Stücker M, Struk A, Altmeyer P, Herde M, Baumgärtl H, Lübbers DW. The cutaneous uptake of atmospheric oxygen contributes significantly to the oxygen supply of human dermis and epidermis. J. Physiol. 2002 Feb;538(Pt 3):985–994.

6. Silver FH, Kato YP, Ohno M, Wasserman AJ. Analysis of mammalian connective tissue: relationship between hierarchical structures and mechanical properties. J. Long. Term Eff. Med. Implants 1992;2(2–3):165–198.

7. Motta P. Ultrastructure of the Connective Tissue Matrix. Springer;2012.

8. Fung YC. Biomechanics: Mechanical Properties of Living Tissues. Springer Science & Business Media; 2013.

9. Elsner P, Berardesca E, Wilhelm K-P. Bioengineering of the Skin: Skin Biomechanics. Taylor & Francis; 2001.

10. Uitto J, Olsen DR, Fazio MJ. Extracellular Matrix of the Skin: 50 Years of Progress. J. Invest. Dermatol. 1989 Apr;92(4, Supplement):S61–S77.

11. Oxlund H, Manschot J, Viidik A. The role of elastin in the mechanical properties of skin. J. Biomech. 1988 Jan;21(3):213–218.

12. Silver FH, Horvath I, Foran DJ. Mechanical Implications of the Domain Structure of Fiber-Forming Collagens: Comparison of the Molecular and Fibrillar Flexibilities of the α1-Chains Found in Types I–III Collagen. J. Theor. Biol. 2002 May;216(2):243–254.

13. Silver FH. Biological materials: structure, mechanical properties, and modeling of soft tissues. 1987.

14. Dunn MG, Silver FH. Viscoelastic behavior of human connective tissues: relative contribution of viscous and elastic components. Connect. Tissue Res. 1983;12(1):59–70.

15. Silver FH, Freeman JW, DeVore D. Viscoelastic properties of human skin and processed dermis. Skin Res. Technol. 2001;7(1):18–23.

16. Silver FH, Christiansen DL, Snowhill PB, Chen Y. Role of storage on changes in the mechanical properties of tendon and self-assembled collagen fibers. Connect. Tissue Res. 2000;41(2):155–164.

17. Kronick PL. Analysis of the effects of pH and tensile deformation on the small-deformation modulus of calf skin. Connect. Tissue Res. 1988;18(2):95–106.

18. Seehra GP, Silver FH. Viscoelastic properties of acid-and alkaline-treated human dermis: a correlation between total surface charge and elastic modulus. Skin Res. Technol. 2006;12(3):190–198.

19. Agache PG, Monneur C, Leveque JL, De Rigal J. Mechanical properties and Young's modulus of human skin in vivo. Arch. Dermatol. Res. 1980;269(3):221–232.

20. Diridollou S, Patat F, Gens F, Vaillant L, Black D, Lagarde JM, Gall Y, Berson M. In vivo model of the mechanical properties of the human skin under suction. Skin Res. Technol. 2000;6(4):214–221.

21. Hendriks FM, Brokken D, van Eemeren JTWM, Oomens CWJ, Baaijens FPT, Horsten JB a. M. A numerical-experimental method to characterize the non-linear mechanical behaviour of human skin. Skin Res. Technol. Off. J. Int. Soc. Bioeng. Skin ISBS Int. Soc. Digit. Imaging Skin ISDIS Int. Soc. Skin Imaging ISSI 2003 Aug;9(3):274–283.

22. Gordon MK, Hahn RA. Collagens. Cell Tissue Res. 2010 Jan;339(1):247–257.

23. Shoulders MD, Raines RT. COLLAGEN STRUCTURE AND STABILITY. Annu. Rev. Biochem. 2009;78:929–958.

24. Parry DA. The molecular and fibrillar structure of collagen and its relationship to the mechanical properties of connective tissue. Biophys. Chem. 1988 Feb;29(1–2):195–209.

25. Silver FH. Mechanosensing and mechanochemical transduction in extracellular matrix: Biological, chemical, engineering, and physiological aspects. Springer Science & Business Media; 2006.

26. Silver FH, Freeman JW, Seehra GP. Collagen self-assembly and the development of tendon mechanical properties. J. Biomech. 2003 Oct;36(10):1529–1553.

27. Silver FH, Bradica G, Tria A. Do changes in mechanical properties of articular cartilage alter mechanochemical transduction and promote osteoarthritis. Matrix Biol 2004;23(7):467–476.

28. Silver FH, Bradica G. Mechanobiology of cartilage: how do internal and external stresses affect mechanochemical transduction and elastic energy storage? Biomech. Model. Mechanobiol. 2002 Dec;1(3):219–238.

29. Wilson AM, McGuigan MP, Su A, van Den Bogert AJ. Horses damp the spring in their step. Nature 2001 Dec;414(6866):895–899.

30. Alexander RM. Elastic Energy Stores in Running Vertebrates. Integr. Comp. Biol. 1984 Feb;24(1):85–94.

31. Biewener AA. Animal Locomotion. OUP Oxford; 2003.

32. Silver FH, DeVore D, Siperko LM. Invited Review: Role of mechanophysiology in aging of ECM: effects of changes in mechanochemical transduction. J. Appl. Physiol. Bethesda Md 1985 2003 Nov;95(5):2134–2141.

33. Hulmes DJ, Jesior JC, Miller A, Berthet-Colominas C, Wolff C. Electron microscopy shows periodic structure in collagen fibril cross sections. Proc. Natl. Acad. Sci. U. S. A. 1981 Jun;78(6):3567–3571.

34. Chattopadhyay S, Raines RT. Review collagen-based biomaterials for wound healing. Biopolymers 2014 Aug;101(8):821–833.

35. Hayashi Y, Yamauchi M, Kim S-K, Kusaoke H. Biomaterials: chitosan and collagen for regenerative medicine. BioMed Res. Int. 2014;2014:690485.

36. Ramshaw J a. M, Vaughan PR, Werkmeister JA. Applications of collagen in medical devices. Biomed. Eng. Appl. Basis Commun. 2001 Feb;13(01):14–26.

37. Wang N, Butler JP, Ingber DE. Mechanotransduction across the cell surface and through the cytoskeleton. Science 1993 May;260(5111):1124–1127.

38. Kjaer M. Role of extracellular matrix in adaptation of tendon and skeletal muscle to mechanical loading. Physiol. Rev. 2004;84(2):649–698.

39. Pearson OM, Lieberman DE. The aging of Wolff's "law": ontogeny and responses to mechanical loading in cortical bone. Am. J. Phys. Anthropol. 2004;125(S39):63–99.

40. Carter DR. Mechanical loading history and skeletal biology. J. Biomech. 1987;20(11–12):1095–1109.

41. Langrana NA, Alexander H, Strauchler I, Metha A, Ricci J. Effect of mechanical load in wound healing. Ann. Plast. Surg. 1983;10(3):200–208.

42. Aarabi S, Bhatt KA, Shi Y, Paterno J, Chang EI, Loh SA, Holmes JW, Longaker MT, Yee H, Gurtner GC. Mechanical load initiates hypertrophic scar formation through decreased cellular apoptosis. FASEB J. 2007;21(12):3250–3261.

43. Levental KR, Yu H, Kass L, Lakins JN, Egeblad M, Erler JT, Fong SF, Csiszar K, Giaccia A, Weninger W. Matrix crosslinking forces tumor progression by enhancing integrin signaling. Cell 2009;139(5):891–906.

44. Yamada H, Evans FG. Strength of biological materials, Ed. 1970.

45. Silver FH. Biomaterials, Medical Devices and Tissue Engineering: An Integrated Approach. Springer, 1994.

46. Brody GS, Peng TJ, Landel RF. The Rheological Properties of Human Skin and Scar Tissues: Bioengineering and the Skin. Int Med Public Lanc. U. K. 1981;

47. Gunner CW, Hutton WC, Burlin TE. The mechanical properties of skin in vivo—a portable hand-held extensometer. Br. J. Dermatol. 1979;100(2):161–163.

48. Wijn PF. The alinear viscoelastic properties of human skin in vivo for small deformations. 1980;

49. Tosti A, Compagno G, Fazzini ML, Villardita S. A ballistometer for the study of the plasto-elastic properties of skin. J. Invest. Dermatol. 1977 Sep;69(3):315–317.

50. Potts RO, Chrisman DA, Buras EM. The dynamic mechanical properties of human skin in vivo. J. Biomech. 1983;16(6):365–372.

51. Hargens C.W. The gas bearing electrodynamometer (GBE) applied to measuring mechanical changes in skin and other tissues. In: Marks R., Payne P.A. (eds) Bioengineering and the Skin. Springer, Dordrecht;(1981).

52. Serup J. Localized scleroderma (morphoea). Clinical, physiological, biochemical and ultrastructural studies with particular reference to quantitation of scleroderma. Acta Derm. Venereol. Suppl. (Stockh.) 1986;122:3–61.

53. Huang Y-P, Zheng Y-P. Measurement of Soft Tissue Elasticity in Vivo: Techniques and Applications. CRC Press; 2015.

54. Artmann GM, Chien S. Bioengineering in Cell and Tissue Research. Springer Science & Business Media; 2008.

55. Nava A, Mazza E, Furrer M, Villiger P, Reinhart WH. In vivo mechanical characterization of human liver. Med. Image Anal. 2008 Apr;12(2):203–216.

56. Urban MW, Nenadic IZ, Chen S, Greenleaf JF. Discrepancies in Reporting Tissue Material Properties. J. Ultrasound Med. Off. J. Am. Inst. Ultrasound Med. 2013 May;32(5):886–888.

57. Kruse SA, Smith JA, Lawrence AJ, Dresner MA, Manduca A, Greenleaf JF, Ehman RL. Tissue characterization using magnetic resonance elastography: preliminary results. Phys. Med. Biol. 2000;45(6):1579.

58. Shah RG, Pierce MC, Silver FH. Morphomechanics of dermis-a method for non-destructive testing of collagenous tissues. Skin Res. Technol. 2017;23(3):399–406.

59. Langer K. On the anatomy and physiology of the skin:I. The cleavability of the cutis. Br. J. Plast. Surg. 1978 Jan;31(1):3–8.

60. Akbal C, Lee SD, Packer SC, Davis MM, Rink RC, Kaefer M. Bladder augmentation with acellular dermal biomatrix in a diseased animal model. J. Urol. 2006 Oct;176(4 Pt 2):1706–1711.

61. Griffin JE, Johnson DL. Management of the maxillofacial burn patient: current therapy. J. Oral Maxillofac. Surg. Off. J. Am. Assoc. Oral Maxillofac. Surg. 2005 Feb;63(2):247–252.

62. Haddock N, Levine J. Breast reconstruction with implants, tissue expanders and AlloDerm: predicting volume and maximizing the skin envelope in skin sparing mastectomies. Breast J. 2010 Feb;16(1):14–19.

63. Gryskiewicz JM, Rohrich RJ, Reagan BJ, Schwartz BM. The Use of AlloDerm for the Correction of Nasal Contour Deformities. Plast. Reconstr. Surg. 2001 Feb;107(2):571.

64. Albo D, Awad SS, Berger DH, Bellows CF. Decellularized human cadaveric dermis provides a safe alternative for primary inguinal hernia repair in contaminated surgical fields. Am. J. Surg. 2006 Nov;192(5):e12-17.

65. Shorr N, Perry JD, Goldberg RA, Hoenig J, Shorr J. The safety and applications of acellular human dermal allograft in ophthalmic plastic and reconstructive surgery: a preliminary report. Ophthal. Plast. Reconstr. Surg. 2000 May;16(3):223–230.

66. Harris RJ. Gingival augmentation with an acellular dermal matrix: human histologic evaluation of a case--placement of the graft on periosteum. Int. J. Periodontics Restorative Dent. 2004 Aug;24(4):378–385.

67. Lee JM, Boughner DR. Mechanical properties of human pericardium. Differences in viscoelastic response when compared with canine pericardium. Circ. Res. 1985 Sep;57(3):475–481.

68. McGuire DA, Hendricks SD. Allograft tissue in ACL reconstruction. Sports Med. Arthrosc. Rev. 2009 Dec;17(4):224–233.

69. Ward RM, Sung VW, Clemons JL, Myers DL. Vaginal paravaginal repair with an AlloDerm graft: Long-term outcomes. Am. J. Obstet. Gynecol. 2007 Dec;197(6):670.e1-5.

70. Moore MA, Samsell B, Wallis G, Triplett S, Chen S, Jones AL, Qin X. Decellularization of human dermis using non-denaturing anionic detergent and endonuclease: a review. Cell Tissue Bank. 2015 Jun;16(2):249–259.

71. Terzini M, Bignardi C, Castagnoli C, Cambieri I, Zanetti EM, Audenino AL. Ex Vivo Dermis Mechanical Behavior in Relation to Decellularization Treatment Length. Open Biomed. Eng. J. 2016;10:34–42.

72. Palmer JE, Russell JP, Grieshober J, Iacangelo A, Ellison BA, Lease TD, Kim H, Henn RF, Hsieh AH. A Biomechanical Comparison of Allograft Tendons for Ligament Reconstruction. Am. J. Sports Med. 2017 Mar;45(3):701–707.

73. Barber FA, Aziz-Jacobo J. Biomechanical testing of commercially available soft-tissue augmentation materials. Arthrosc. J. Arthrosc. Relat. Surg. Off. Publ. Arthrosc. Assoc. N. Am. Int. Arthrosc. Assoc. 2009 Nov;25(11):1233–1239.

74. Fercher AF, Drexler W, Hitzenberger CK, Lasser T. Optical coherence tomography-principles and applications. Rep. Prog. Phys. 2003;66(2):239.

75. Huang D, Swanson EA, Lin CP, Schuman JS, Stinson WG, Chang W, Hee MR, Flotte T, Gregory K, Puliafito CA. Optical coherence tomography. Sci. N. Y. NY 1991;254(5035):1178.

76. Hee MR, Puliafito CA, Wong C, Duker JS, Reichel E, Rutledge B, Schuman JS, Swanson EA, Fujimoto JG. Quantitative assessment of macular edema with optical coherence tomography. Arch. Ophthalmol. 1995;113(8):1019–1029.

77. Escobar PF, Belinson JL, White A, Shakhova NM, Feldchtein FI, Kareta MV, Gladkova ND. Diagnostic efficacy of optical coherence tomography in the management of preinvasive and invasive cancer of uterine cervix and vulva. Int. J. Gynecol. Cancer 2004;14(3):470–474.

78. Gladkova ND, Petrova GA, Nikulin NK, Radenska-Lopovok SG, Snopova LB, Chumakov YP, Nasonova VA, Gelikonov VM, Gelikonov GV, Kuranov RV. In vivo optical coherence tomography imaging of human skin: norm and pathology. Skin Res. Technol. 2000;6(1):6–16.

79. Fujimoto JG, Pitris C, Boppart SA, Brezinski ME. Optical coherence tomography: an emerging technology for biomedical imaging and optical biopsy. Neoplasia 2000;2(1–2):9–25.

80. Fujimoto JG, Brezinski ME, Tearney GJ, Boppart SA, Bouma B, Hee MR, Southern JF, Swanson EA. Optical biopsy and imaging using optical coherence tomography. Nat. Med. 1995;1(9):970–972.

81. Chen TC, Cense B, Pierce MC, Nassif N, Park BH, Yun SH, White BR, Bouma BE, Tearney GJ, de Boer JF. Spectral domain optical coherence tomography: ultra-high speed, ultra-high resolution ophthalmic imaging. Arch. Ophthalmol. 2005;123(12):1715–1720.

82. Bouma BE, Yun S-H, Vakoc BJ, Suter MJ, Tearney GJ. Fourier-domain optical coherence tomography: recent advances toward clinical utility. Curr. Opin. Biotechnol. 2009;20(1):111–118.

83. Choma MA, Sarunic MV, Yang C, Izatt JA. Sensitivity advantage of swept source and Fourier domain optical coherence tomography. Opt. Express 2003;11(18):2183–2189.

84. Fercher AF, Hitzenberger CK, Kamp G, El-Zaiat SY. Measurement of intraocular distances by backscattering spectral interferometry. Opt. Commun. 1995;117(1–2):43–48.

85. Silver FH, Shah R. Measurement of mechanical properties of natural and engineered implants. Adv Tissue Eng Regen Med 2016;1:00004.

86. Manduca A, Oliphant TE, Dresner MA, Mahowald JL, Kruse SA, Amromin E, Felmlee JP, Greenleaf JF, Ehman RL. Magnetic resonance elastography: non-invasive mapping of tissue elasticity. Med. Image Anal. 2001;5(4):237–254.

87. Muthupillai R, Lomas DJ, Rossman PJ, Greenleaf JF, Manduca A, Ehman RL. Magnetic resonance elastography by direct visualization of propagating acoustic strain waves. science 1995;269(5232):1854–1857.

88. De Korte CL, Pasterkamp G, Van Der Steen AF, Woutman HA, Bom N. Characterization of plaque components with intravascular ultrasound elastography in human femoral and coronary arteries in vitro. Circulation 2000;102(6):617–623.

89. Zhi H, Ou B, Luo B-M, Feng X, Wen Y-L, Yang H-Y. Comparison of ultrasound elastography, mammography, and sonography in the diagnosis of solid breast lesions. J. Ultrasound Med. 2007;26(6):807–815.

90. Tearney GJ, Brezinski ME, Southern JF, Bouma BE, Boppart SA, Fujimoto JG. Optical biopsy in human gastrointestinal tissue using optical coherence tomography. Am. J. Gastroenterol. 1997;92(10)

91. Liang X, Boppart SA. Biomechanical properties of in vivo human skin from dynamic optical coherence elastography. IEEE Trans. Biomed. Eng. 2010;57(4):953–959.

92. Ophir J, Cespedes I, Ponnekanti H, Yazdi Y, Li X. Elastography: a quantitative method for imaging the elasticity of biological tissues. Ultrason. Imaging 1991;13(2):111–134.

93. Sandrin L, Fourquet B, Hasquenoph J-M, Yon S, Fournier C, Mal F, Christidis C, Ziol M, Poulet B, Kazemi F. Transient elastography: a new noninvasive method for assessment of hepatic fibrosis. Ultrasound Med. Biol. 2003;29(12):1705–1713.

94. Wojcinski S, Farrokh A, Weber S, Thomas A, Fischer T, Slowinski T, Schmidt W, Degenhardt F. Multicenter study of ultrasound real-time tissue elastography in 779 cases for the assessment of breast lesions: improved diagnostic performance by combining the BI-RADS®-US classification system with sonoelastography. Ultraschall Med.-Eur. J. Ultrasound 2010;31(05):484–491.

95. Righetti R, Srinivasan S, Ophir J. Lateral resolution in elastography. Ultrasound Med. Biol. 2003;29(5):695–704.

96. Barton MB, Harris R, Fletcher SW. The rational clinical examination. Does this patient have breast cancer? The screening clinical breast examination: should it be done? How? JAMA 1999 Oct;282(13):1270–1280.

97. Elias D, Sideris L, Pocard M, de Baere T, Dromain C, Lassau N, Lasser P. Incidence of unsuspected and treatable metastatic disease associated with operable colorectal liver metastases discovered only at laparotomy (and not treated when performing percutaneous radiofrequency ablation). Ann. Surg. Oncol. 2005 Apr;12(4):298–302.

98. Yin M, Glaser KJ, Talwalkar JA, Chen J, Manduca A, Ehman RL. Hepatic MR Elastography: Clinical Performance in a Series of 1377 Consecutive Examinations. Radiology 2016 Jan;278(1):114–124.

99. Green MA, Bilston LE, Sinkus R. In vivo brain viscoelastic properties measured by magnetic resonance elastography. NMR Biomed. 2008 Aug;21(7):755–764.

100. Ringleb SI, Bensamoun SF, Chen Q, Manduca A, An K-N, Ehman RL. Applications of magnetic resonance elastography to healthy and pathologic skeletal muscle. J. Magn. Reson. Imaging JMRI 2007 Feb;25(2):301–309.

101. McKnight AL, Kugel JL, Rossman PJ, Manduca A, Hartmann LC, Ehman RL. MR elastography of breast cancer: preliminary results. AJR Am. J. Roentgenol. 2002 Jun;178(6):1411–1417.

102. Mariappan YK, Glaser KJ, Ehman RL. Magnetic resonance elastography: a review. Clin. Anat. N. Y. N 2010 Jul;23(5):497–511.

103. Chen J, Yin M, Glaser KJ, Talwalkar JA, Ehman RL. MR Elastography of Liver Disease: State of the Art. Appl. Radiol. 2013 Apr;42(4):5–12.

104. Rotsch C, Radmacher M. Drug-induced changes of cytoskeletal structure and mechanics in fibroblasts: an atomic force microscopy study. Biophys. J. 2000 Jan;78(1):520–535.

105. Costa KD. Single-cell elastography: probing for disease with the atomic force microscope. Dis. Markers 2003 2004;19(2–3):139–154.

106. Kuznetsova TG, Starodubtseva MN, Yegorenkov NI, Chizhik SA, Zhdanov RI. Atomic force microscopy probing of cell elasticity. Micron Oxf. Engl. 1993 2007;38(8):824–833.

107. Kirmizis D, Logothetidis S. Atomic force microscopy probing in the measurement of cell mechanics. Int. J. Nanomedicine 2010 Apr;5:137–145.

108. Garra BS. Elastography: history, principles, and technique comparison. Abdom. Imaging 2015 Apr;40(4):680–697.

109. Nightingale K. Acoustic Radiation Force Impulse (ARFI) Imaging: a Review. Curr. Med. Imaging Rev. 2011 Nov;7(4):328–339.

110. Bouillard K, Nordez A, Hug F. Estimation of Individual Muscle Force Using Elastography. PLOS ONE 2011 Dec;6(12):e29261.

111. Shiina T, Nightingale KR, Palmeri ML, Hall TJ, Bamber JC, Barr RG, Castera L, Choi BI, Chou Y-H, Cosgrove D, Dietrich CF, Ding H, Amy D, Farrokh A, Ferraioli G, Filice C, Friedrich-Rust M, Nakashima K, Schafer F, Sporea I, Suzuki S, Wilson S, Kudo M. WFUMB Guidelines and Recommendations for Clinical Use of Ultrasound Elastography: Part 1: Basic Principles and Terminology. Ultrasound Med. Biol. 2015 May;41(5):1126–1147.

112. Bamber J, Cosgrove D, Dietrich CF, Fromageau J, Bojunga J, Calliada F, Cantisani V, Correas J-M, D'Onofrio M, Drakonaki EE, Fink M, Friedrich-Rust M, Gilja OH, Havre RF, Jenssen C, Klauser AS, Ohlinger R, Saftoiu A, Schaefer F, Sporea I, Piscaglia F. EFSUMB guidelines and recommendations on the clinical use of ultrasound elastography. Part 1: Basic principles and technology. Ultraschall Med. Stuttg. Ger. 1980 2013 Apr;34(2):169–184.

113. Righetti R, Ophir J, Ktonas P. Axial resolution in elastography. Ultrasound Med. Biol. 2002 Jan;28(1):101–113.

114. Thitaikumar A, Righetti R, Krouskop TA, Ophir J. Resolution of axial shear strain elastography. Phys. Med. Biol. 2006 Oct;51(20):5245–5257.

115. Sigrist RMS, Liau J, Kaffas AE, Chammas MC, Willmann JK. Ultrasound Elastography: Review of Techniques and Clinical Applications. Theranostics 2017 Mar;7(5):1303–1329.

116. Qiu Y, Wang Y, Xu Y, Chandra N, Haorah J, Hubbi B, Pfister BJ, Liu X. Quantitative optical coherence elastography based on fiber-optic probe for in situ measurement of tissue mechanical properties. Biomed. Opt. Express 2016 Jan;7(2):688–700.

117. Ahmad A, Huang P-C, Sobh NA, Pande P, Kim J, Boppart SA. Mechanical contrast in spectroscopic magnetomotive optical coherence elastography. Phys. Med. Biol. 2015;60(17):6655.

118. Kennedy KM, Chin L, McLaughlin RA, Latham B, Saunders CM, Sampson DD, Kennedy BF. Quantitative micro-elastography: imaging of tissue elasticity using compression optical coherence elastography. Sci. Rep. 2015;5

119. Wang S, Larin KV. Optical coherence elastography for tissue characterization: a review. J. Biophotonics 2015;8(4):279–302.

120. Larin KV, Sampson DD. Optical coherence elastography–OCT at work in tissue biomechanics. Biomed. Opt. Express 2017;8(2):1172–1202.

121. Wells PN, Liang H-D. Medical ultrasound: imaging of soft tissue strain and elasticity. J. R. Soc. Interface 2011;8(64):1521–1549.

122. Kennedy KM, Es'haghian S, Chin L, McLaughlin RA, Sampson DD, Kennedy BF. Optical palpation: optical coherence tomography-based tactile imaging using a compliant sensor. Opt. Lett. 2014;39(10):3014–3017.

123. Orescanin M, Toohey KS, Insana MF. Material properties from acoustic radiation force step response. J. Acoust. Soc. Am. 2009;125(5):2928–2936.

124. Sticker M, Hitzenberger CK, Leitgeb R, Fercher AF. Quantitative differential phase measurement and imaging in transparent and turbid media by optical coherence tomography. Opt. Lett. 2001;26(8):518–520.

125. Zaitsev VY, Matveyev AL, Matveev LA, Gelikonov GV, Gelikonov VM, Vitkin A. Deformation-induced speckle-pattern evolution and feasibility of correlational

speckle tracking in optical coherence elastography. J. Biomed. Opt. 2015;20(7):075006–075006.

126. Schmitt JM. OCT elastography: imaging microscopic deformation and strain of tissue. Opt. Express 1998 Sep;3(6):199–211.

127. Kennedy BF, Kennedy KM, Sampson DD. A review of optical coherence elastography: fundamentals, techniques and prospects. IEEE J. Sel. Top. Quantum Electron. 2014;20(2):272–288.

128. Ford MR, Sinha Roy A, Rollins AM, Dupps WJ. Serial biomechanical comparison of edematous, normal, and collagen crosslinked human donor corneas using optical coherence elastography. J. Cataract Refract. Surg. 2014 Jun;40(6):1041–1047.

129. Armstrong BK, Lin MP, Ford MR, Santhiago MR, Singh V, Grossman GH, Agrawal V, Sinha RA, Butler RS, Dupps WJ, Wilson SE. Biological and biomechanical responses to traditional epithelium-off and transepithelial riboflavin-UVA CXL techniques in rabbits. J. Refract. Surg. Thorofare NJ 1995 2013;29(5):332–341.

130. Ford MR, Dupps WJ, Rollins AM, Sinha RA, Hu Z. Method for optical coherence elastography of the cornea. J. Biomed. Opt. 2011 Feb;16(1):016005.

131. Li C, Guan G, Reif R, Huang Z, Wang RK. Determining elastic properties of skin by measuring surface waves from an impulse mechanical stimulus using phase-sensitive optical coherence tomography. J. R. Soc. Interface 2012 May;9(70):831–841.

132. Kennedy KM, McLaughlin RA, Kennedy BF, Tien A, Latham B, Saunders CM, Sampson DD. Needle optical coherence elastography for the measurement of microscale mechanical contrast deep within human breast tissues. J. Biomed. Opt. 2013 Dec;18(12):121510.

133. Kennedy KM, Kennedy BF, McLaughlin RA, Sampson DD. Needle optical coherence elastography for tissue boundary detection. Opt. Lett. 2012 Jun;37(12):2310–2312.

134. Qi W, Chen R, Chou L, Liu G, Zhang J, Zhou Q, Chen Z. Phase-resolved acoustic radiation force optical coherence elastography. J. Biomed. Opt. 2012 Nov;17(11):110505.

135. Liang X, Orescanin M, Toohey KS, Insana MF, Boppart SA. Acoustomotive optical coherence elastography for measuring material mechanical properties. Opt. Lett. 2009 Oct;34(19):2894–2896.

136. Guan G, Li C, Ling Y, Yang Y, Vorstius JB, Keatch RP, Wang RK, Huang Z. Quantitative evaluation of degenerated tendon model using combined optical coherence elastography and acoustic radiation force method. J. Biomed. Opt. 2013 Nov;18(11):111417.

137. Razani M, Mariampillai A, Sun C, Luk TWH, Yang VXD, Kolios MC. Feasibility of optical coherence elastography measurements of shear wave propagation in

homogeneous tissue equivalent phantoms. Biomed. Opt. Express 2012 May;3(5):972–980.

138. Nguyen T-M, Song S, Arnal B, Huang Z, O'Donnell M, Wang RK. Visualizing ultrasonically induced shear wave propagation using phase-sensitive optical coherence tomography for dynamic elastography. Opt. Lett. 2014 Feb;39(4):838–841.

139. Qi W, Li R, Ma T, Li J, Kirk Shung K, Zhou Q, Chen Z. Resonant acoustic radiation force optical coherence elastography. Appl. Phys. Lett. 2013 Sep;103(10):103704.

140. Xu X, Zhu J, Chen Z. Dynamic and quantitative assessment of blood coagulation using optical coherence elastography. Sci. Rep. 2016 Apr;6:24294.

141. Ejofodomi OA, Zderic V, Zara JM. Development of novel imaging probe for optical/acoustic radiation imaging (OARI). Med. Phys. 2013 Nov;40(11):111910.

142. Razani M, Luk TWH, Mariampillai A, Siegler P, Kiehl T-R, Kolios MC, Yang VXD. Optical coherence tomography detection of shear wave propagation in inhomogeneous tissue equivalent phantoms and ex-vivo carotid artery samples. Biomed. Opt. Express 2014 Mar;5(3):895–906.

143. Nguyen T-M, Arnal B, Song S, Huang Z, Wang RK, O'Donnell M. Shear wave elastography using amplitude-modulated acoustic radiation force and phase-sensitive optical coherence tomography. J. Biomed. Opt. 2015 Jan;20(1):016001.

144. Ambroziński Ł, Song S, Yoon SJ, Pelivanov I, Li D, Gao L, Shen TT, Wang RK, O'Donnell M. Acoustic micro-tapping for non-contact 4D imaging of tissue elasticity. Sci. Rep. 2016 Dec;6:38967.

145. Ambroziński Ł, Pelivanov I, Song S, Yoon SJ, Li D, Gao L, Shen TT, Wang RK, O'Donnell M. Air-coupled acoustic radiation force for non-contact generation of broadband mechanical waves in soft media. Appl. Phys. Lett. 2016 Jul;109(4):043701.

146. Han Z, Aglyamov SR, Li J, Singh M, Wang S, Vantipalli S, Wu C, Liu C-H, Twa MD, Larin KV. Quantitative assessment of corneal viscoelasticity using optical coherence elastography and a modified Rayleigh-Lamb equation. J. Biomed. Opt. 2015 Feb;20(2):20501.

147. Wang S, Larin KV. Noncontact depth-resolved micro-scale optical coherence elastography of the cornea. Biomed. Opt. Express 2014 Nov;5(11):3807–3821.

148. Du Y, Liu C-H, Lei L, Singh M, Li J, Hicks MJ, Larin KV, Mohan C. Rapid, noninvasive quantitation of skin disease in systemic sclerosis using optical coherence elastography. J. Biomed. Opt. 2016 Apr;21(4):46002.

149. Wang S, Lopez AL, Morikawa Y, Tao G, Li J, Larina IV, Martin JF, Larin KV. Noncontact quantitative biomechanical characterization of cardiac muscle using shear wave imaging optical coherence tomography. Biomed. Opt. Express 2014 Jul;5(7):1980–1992.

150. Wang S, Li J, Manapuram RK, Menodiado FM, Ingram DR, Twa MD, Lazar AJ, Lev DC, Pollock RE, Larin KV. Noncontact measurement of elasticity for the detection of soft-tissue tumors using phase-sensitive optical coherence tomography combined with a focused air-puff system. Opt. Lett. 2012 Dec;37(24):5184–5186.

151. Liu C-H, Du Y, Singh M, Wu C, Han Z, Li J, Chang A, Mohan C, Larin KV. Classifying murine glomerulonephritis using optical coherence tomography and optical coherence elastography. J. Biophotonics 2016 Aug;9(8):781–791.

152. Wu C, Singh M, Han Z, Raghunathan R, Liu CH, Li J, Schill A, Larin KV. Lorentz force optical coherence elastography. J. Biomed. Opt. J. Biomed. Opt. 2016 Sep;21, 21(9, 9):90502–90502.

153. Crecea V, Oldenburg AL, Liang X, Ralston TS, Boppart SA. Magnetomotive nanoparticle transducers for optical rheology of viscoelastic materials. Opt. Express 2009 Dec;17(25):23114–23122.

154. Oldenburg AL, Boppart SA. Resonant acoustic spectroscopy of soft tissues using embedded magnetomotive nanotransducers and optical coherence tomography. Phys. Med. Biol. 2010;55(4):1189.

155. Ahmad A, Kim J, Sobh NA, Shemonski ND, Boppart SA. Magnetomotive optical coherence elastography using magnetic particles to induce mechanical waves. Biomed. Opt. Express 2014 Jun;5(7):2349–2361.

156. Özkaya, N., Nordin, M., Goldsheyder, D., & Leger, D.. Fundamentals of Biomechanics: Equilibrium, Motion, and Deformation. Springer Science & Business Media. (2012).

157. Liang X, Oldenburg AL, Crecea V, Chaney EJ, Boppart SA. Optical micro-scale mapping of dynamic biomechanical tissue properties. Opt. Express 2008 Jul;16(15):11052–11065.

158. Wang S, Aglyamov S, Karpiouk A, Li J, Emelianov S, Manns F, Larin KV. Assessing the mechanical properties of tissue-mimicking phantoms at different depths as an approach to measure biomechanical gradient of crystalline lens. Biomed. Opt. Express 2013;4(12):2769–2780.

159. Yue X, Wang L, Wang R. Tissue Modeling and Analyzing with Finite Element Method: A Review for Cranium Brain Imaging [Internet]. Int. J. Biomed. Imaging 2013;

160. Liang X, Crecea V, Boppart Sa. Dynamic Optical Coherence Elastography: A Review. J. Innov. Opt. Health Sci. 2010 Oct;3(4):221–233.

161. Liang X, Adie SG, John R, Boppart SA. Dynamic spectral-domain optical coherence elastography for tissue characterization. Opt. Express 2010 Jun;18(13):14183–14190.

162. Adie SG, Liang X, Kennedy BF, John R, Sampson DD, Boppart SA. Spectroscopic optical coherence elastography. Opt. Express 2010 Dec;18(25):25519–25534.

163. Tanter M, Bercoff J, Athanasiou A, Deffieux T, Gennisson J-L, Montaldo G, Muller M, Tardivon A, Fink M. Quantitative assessment of breast lesion viscoelasticity: initial clinical results using supersonic shear imaging. Ultrasound Med. Biol. 2008;34(9):1373–1386.

164. Protsenko DE, Zemek A, Wong BJ. Temperature dependent change in equilibrium elastic modulus after thermally induced stress relaxation in porcine septal cartilage. Lasers Surg. Med. 2008;40(3):202–210.

165. Mueller S, Sandrin L. Liver stiffness: a novel parameter for the diagnosis of liver disease. Hepatic Med. Evid. Res. 2010;2:49.

166. Wollensak G, Spoerl E, Seiler T. Stress-strain measurements of human and porcine corneas after riboflavin–ultraviolet-A-induced cross-linking. J. Cataract Refract. Surg. 2003;29(9):1780–1785.

167. Choi S, Lee H-J, Cheong Y, Shin J-H, Jin K-H, Park H-K, Park Y-G. AFM study for morphological characteristics and biomechanical properties of human cataract anterior lens capsules. Scanning 2012;34(4):247–256.

168. Silver FH, Christiansen DL. Biomaterials science and biocompatibility. Springer Science & Business Media; 1999.

169. Kalath S, Tsipouras P, Silver FH. Increased aortic root stiffness associated with osteogenesis imperfecta. Ann. Biomed. Eng. 1987;15(1):91–99.

170. Dudea SM, Dumitriu D, Vasilescu D, Manole S, Lenghel M. Differentiating benign from malignant superficial lymph nodes with sonoelastography. Med. Ultrason. 2013;15(2):132–139.

171. Salafia CM, Yampolsky M, Shlakhter A, Mandel DH, Schwartz N. Variety in placental shape: when does it originate? Placenta 2012 Mar;33(3):164–170.

172. Straughen J, Salafia C, Perez-Avilan G, Onbreyt V, Shah R, Devine-Dunn A, Dygulska B, Lederman S, Narula P, Misra D. Prenatal placental inflammatory exposures as measured by routine placental histopathology in a community cohort of ASD. Placenta 2016;45:90.

173. Daskalakis G, Marinopoulos S, Krielesi V, Papapanagiotou A, Papantoniou N, Mesogitis S, Antsaklis A. Placental pathology in women with gestational diabetes. Acta Obstet. Gynecol. Scand. 2008;87(4):403–407.

174. King BF, Blankenship TN. Differentiation of the chorionic plate of the placenta: Cellular and extracellular matrix changes during development in the macaque. Anat. Rec. 1994;240(2):267–276.

175. Sage H, Woodbury RG, Bornstein P. Structural studies on human type IV collagen. J. Biol. Chem. 1979;254(19):9893–9900.

176. Niyibizi C, Fietzek PP, Van der Rest M. Human placenta type V collagens. Evidence for the existence of an alpha 1 (V) alpha 2 (V) alpha 3 (V) collagen molecule. J. Biol. Chem. 1984;259(22):14170–14174.

177. Benirschke K, Driscoll SG. The pathology of the human placenta. In: Placenta. Springer; 1967 p. 97–571.

178. McAleavey SA, Parker KJ, Ormachea J, Wood RW, Stodgell CJ, Katzman PJ, Pressman EK, Miller RK. Shear wave elastography in the living, perfused, post-delivery placenta. Ultrasound Med. Biol. 2016;42(6):1282–1288.

179. Pain HJ, Pain HJ. The physics of vibrations and waves. Wiley Online Library; 1999.

180. Del Río LM, López F, Calleja B, Tejado JJ, Mota MI, González I, San Emeterio JL, Ramos A. Antonio; Resonance-based acoustic technique applied to the determination of Young's modulus in granites. In: 19th Internacional Congress on Acoustics, Madrid September. 2007

181. Rosell JR, Cantalapiedra IR. Simple method of dynamic Young's modulus determination in lime and cement mortars. Mater. Constr. 2011;61(301):39–48.

182. Revel GM, Scalise A, Scalise L. Vibrational analysis of tendons' mechanical properties. In: Fifth International Conference on Vibration Measurements by Laser Techniques: Advances and Applications. International Society for Optics and Photonics; 2002 p. 168–180.

183. Silver FH, Silver L, Shah R. Viscoelastic Behavior of Allografts and Scaffolds Composed of Extracellular Matrices. Adv Tissue Eng Regen Med 2017 Feb;2(1)

184. Dunn MG, Silver FH, Swann DA. Mechanical analysis of hypertrophic scar tissue: structural basis for apparent increased rigidity. J. Invest. Dermatol. 1985 Jan;84(1):9–13.

185. Agache P, Humbert P. Measuring the Skin. Springer Science & Business Media; 2004.

186. Escoffier C, de Rigal J, Rochefort A, Vasselet R, Léveˆque J-L, Agache PG. Age-related mechanical properties of human skin: An in vivo study. J. Invest. Dermatol. 1989 Sep;93(3):353–357.

187. Daniel Macias J, Ordonez-Miranda J, Alvarado-Gil JJ. Resonance frequencies and Young's modulus determination of magnetorheological elastomers using the photoacoustic technique. J. Appl. Phys. 2012 Dec;112(12):124910.

188. Singh B, Nanda BK. Estimation of Damping in Layered Welded Structures with Unequal Thickness. Shock Vib. 2012;

189. Macioce P. Viscoelastic damping 101. Sound and Vibration Magazine. 2003(4):4-5.

190. Papagiannopoulos GA, Hatzigeorgiou GD. On the use of the half-power bandwidth method to estimate damping in building structures. Soil Dyn. Earthq. Eng. 2011;31(7):1075–1079.

191. Pereira JM, Mansour JM, Davis BR. Dynamic measurement of the viscoelastic properties of skin. J. Biomech. 1991;24(2):157–162.

192. Sasaki N, Shukunami N, Matsushima N, Izumi Y. Time-resolved X-ray diffraction from tendon collagen during creep using synchrotron radiation. J. Biomech. 1999 Mar;32(3):285–292.

193. Folkard W, Geercken W, Knörzer E, Mosler E, Nemetschek-Gansler H, Nemetschek T, Koch MH. Structural dynamic of native tendon collagen. J. Mol. Biol. 1987 Jan;193(2):405–407.

194. Notarnicola A, Moretti B. The biological effects of extracorporeal shock wave therapy (eswt) on tendon tissue. Muscles Ligaments Tendons J. 2012 Jun;2(1):33–37.

195. Jones CJ, Fox H. Ultrastructure of the normal human placenta. Electron Microsc. Rev. 1991;4(1):129–178.

196. Serov AS, Salafia CM, Brownbill P, Grebenkov DS, Filoche M. Optimal villi density for maximal oxygen uptake in the human placenta. J. Theor. Biol. 2015 Jan;364:383–396.

197. Higgins M, Felle P, Mooney EE, Bannigan J, McAuliffe FM. Stereology of the placenta in type 1 and type 2 diabetes. Placenta 2011;32(8):564–569.

198. Salgado SS, Salgado MKR. Structural changes in pre-eclamptic and eclamptic placentas—an ultrastructural study. J Coll Physicians Surg Pak 2011;21(8):482–486.

199. Baptiste-Roberts K, Salafia CM, Nicholson WK, Duggan A, Wang N-Y, Brancati FL. Maternal risk factors for abnormal placental growth: the national collaborative perinatal project. BMC Pregnancy Childbirth 2008 Sep;8:44.

200. Strøm-Roum EM, Haavaldsen C, Tanbo TG, Eskild A. Placental weight relative to birthweight in pregnancies with maternal diabetes mellitus. Acta Obstet. Gynecol. Scand. 2013 Jul;92(7):783–789.

201. Hoying JB, Utzinger U, Weiss JA. Formation of microvascular networks: role of stromal interactions directing angiogenic growth. Microcirculation 2014;21(4):278–289.

202. Senger DR, Davis GE. Angiogenesis. Cold Spring Harb. Perspect. Biol. 2011;3(8):a005090.

203. Edgar LT. The dynamic biomechanical regulation of morphogenesis. The University of Utah; 2015.

204. Pressman EK, Cavanaugh JL, Woods JR. Physical properties of the chorioamnion throughout gestation. Am. J. Obstet. Gynecol. 2002 Sep;187(3):672–675.

205. Kruskal WH, Wallis WA. Use of Ranks in One-Criterion Variance Analysis. J. Am. Stat. Assoc. 1952 Dec;47(260):583–621.

206. Welch BL. On the Comparison of Several Mean Values: An Alternative Approach. Biometrika 1951;38(3/4):330–336.

207. Manoogian SJ, Bisplinghoff JA, McNally C, Kemper AR, Santago AC, Duma SM. Dynamic tensile properties of human placenta. J. Biomech. 2008 Jan;41:3436–3440.

208. Alan B, Göya C, Tunç S, Teke M, Hattapoğlu S. Assessment of Placental Stiffness Using Acoustic Radiation Force Impulse Elastography in Pregnant Women with Fetal Anomalies. Korean J. Radiol. 2016;17(2):218–223.

209. Karaman E, Arslan H, Çetin O, Şahin HG, Bora A, Yavuz A, Elasan S, Akbudak İ. Comparison of placental elasticity in normal and pre-eclamptic pregnant women by acoustic radiation force impulse elastosonography. J. Obstet. Gynaecol. Res. 2016 Nov;42(11):1464–1470.

210. Dodson RB, Martin JT, Hunter KS, Ferguson VL. Determination of hyperelastic properties for umbilical artery in preeclampsia from uniaxial extension tests. Eur. J. Obstet. Gynecol. 2013 Jul;169:207–212.

211. Geva E, Ginzinger DG, Zaloudek CJ, Moore DH, Byrne A, Jaffe RB. Human Placental Vascular Development: Vasculogenic and Angiogenic (Branching and Nonbranching) Transformation Is Regulated by Vascular Endothelial Growth Factor-A, Angiopoietin-1, and Angiopoietin-2. J. Clin. Endocrinol. Metab. 2002 Sep;87(9):4213–4224.

212. Gersell DJ. Chronic villitis, chronic chorioamnionitis, and maternal floor infarction. Semin. Diagn. Pathol. 1993 Aug;10(3):251–266.

213. Katzman PJ. Chronic inflammatory lesions of the placenta. Semin. Perinatol. 2015 Feb;39(1):20–26.

214. Burton GJ, Fowden AL, Thornburg KL. Placental Origins of Chronic Disease. Physiol. Rev. 2016 Oct;96(4):1509–1565.

215. Roberts DJ, Celi AC, Riley LE, Onderdonk AB, Boyd TK, Johnson LC, Lieberman E. Acute histologic chorioamnionitis at term: nearly always noninfectious. PloS One 2012;7(3):e31819.

216. Intrapartum Management of Intraamniotic Infection - ACOG Committee Opinion Number 712; August 2017.

217. Arioz Habibi H, Alici Davutoglu E, Kandemirli SG, Aslan M, Ozel A, Kalyoncu Ucar A, Zeytun P, Madazli R, Adaletli I. In vivo assessment of placental elasticity in

intrauterine growth restriction by shear-wave elastography. Eur. J. Radiol. 2017 Dec;97:16–20.

218. Kakabadze Z, Mardaleishvili K, Loladze G, Javakhishvili I, Chakhunasvili K, Karalashvili L, Sukhitashvili N, Chutkerashvili G, Kakabadze A, Chakhunasvili D. Clinical application of decellularized and lyophilized human amnion/chorion membrane grafts for closing post-laryngectomy pharyngocutaneous fistulas. J. Surg. Oncol. 2016 Apr;113(5):538–543.

219. Choi JS, Kim JD, Yoon HS, Cho YW. Full-Thickness Skin Wound Healing Using Human Placenta-Derived Extracellular Matrix Containing Bioactive Molecules. Tissue Eng. Part A 2013 Feb;19(3–4):329–339.

220. Kong M-H, Lee E-J, Lee S-Y, Cho S-J, Hong Y-S, Park S-B. Effect of human placental extract on menopausal symptoms, fatigue, and risk factors for cardiovascular disease in middle-aged Korean women. Menopause N. Y. N 2008 Apr;15(2):296–303.

221. Kong M, Park SB. Effect of human placental extract on health status in elderly koreans. Evid.-Based Complement. Altern. Med. ECAM 2012;2012:732915.

222. Pöschl E, Schlötzer-Schrehardt U, Brachvogel B, Saito K, Ninomiya Y, Mayer U. Collagen IV is essential for basement membrane stability but dispensable for initiation of its assembly during early development. Development 2004 Apr;131(7):1619–1628.